A ONE DIMENSIONAL SLOT MODE PHOTONIC CRYSTAL NANOBEAM CAVITY DESIGN FOR OPTICAL BIO-SENSING APPLICATIONS

A THESIS SUBMITTED TO
THE GRADUATE SCHOOL OF NATURAL AND APPLIED SCIENCES
OF
MIDDLE EAST TECHNICAL UNIVERSITY

BY

MERTCAN ERDİL

IN PARTIAL FULFILLMENT OF THE REQUIREMENTS
FOR
THE DEGREE OF MASTER OF SCIENCE
IN
ELECTRICAL AND ELECTRONIC ENGINEERING

JULY 2020

Approval of the thesis:

A ONE DIMENSIONAL SLOT MODE PHOTONIC CRYSTAL NANOBEAM CAVITY DESIGN FOR OPTICAL BIO-SENSING APPLICATIONS

submitted by **MERTCAN ERDİL** in partial fulfillment of the requirements for the degree of **Master of Science in Electrical and Electronic Engineering, Middle East Technical University** by,

Prof. Dr. Halil Kalıpçılar
Dean, Graduate School of **Natural and Applied Sciences** _____

Prof. Dr. İlkay Ulusoy
Head of the Department, **Electrical & Electronics Eng.** _____

Assoc. Prof. Dr. Serdar Kocaman
Supervisor, **Electrical & Electronics Eng., METU** _____

Examining Committee Members:

Prof. Dr. Gönül Turhan Sayan
Electrical and Electronics Eng., METU _____

Assoc. Prof. Dr. Serdar Kocaman
Electrical and Electronics Eng., METU _____

Prof. Dr. Haluk Külah
Electrical and Electronics Eng., METU _____

Prof. Dr. Hamza Kurt
Electrical and Electronics Eng., TOBB ETU. _____

Asst. Prof. Dr. Emre Yüce
Physics, METU _____

Date: 23.07.2020

I hereby declare that all information in this document has been obtained and presented in accordance with academic rules and ethical conduct. I also declare that, as required by these rules and conduct, I have fully cited and referenced all material and results that are not original to this work.

Name, Last name : Mertcan, Erdil

Signature:

ABSTRACT

A ONE DIMENSIONAL SLOT MODE PHOTONIC CRYSTAL NANOBEAM CAVITY DESIGN FOR OPTICAL BIO-SENSING APPLICATIONS

Erdil, Mertcan
Master of Science, Electrical and Electronic Engineering
Supervisor: Assoc. Prof. Dr. Serdar Kocaman

July 2020, 82 pages

In this thesis, we presented a refractive index based optical bio-sensor, utilizing a slot mode one dimensional photonic crystal cavity as a transducing element. We benefited from the suitability of slotted one dimensional photonic crystal cavities for optical bio-sensing applications, owing to their capability of confining the light strongly in the low dielectric media. We described the theory behind the design, and also provided numerical analyses, characterizing the device performance. We also demonstrated a performance enhancement method, relying on an optomechanical feedback loop, which can enhance both the quality factor and the sensitivity of the resonant cavity. The enhancement mechanism is triggered when the target analyte enters the background medium and modifies the cavity slot width, by benefiting from the optical transverse gradient forces inside the cavity. By the help of the optomechanical feedback loop, the intrinsic trade-off between the performance factors can be eliminated, resulting in an improved figure of merit. In the thesis, we demonstrated the operation principle of the enhancement method, together with the numerical calculations necessary for the investigation of the level of enhancement. Our optomechanical feedback loop can be appended to any resonant structure

without any modification, proposing a strong potential for our enhancement method to be utilized in other refractive index based optical bio-sensing schemes.

Keywords: Optomechanical Enhancement, Photonic Crystal Cavity, Refractive Index Sensing, Slot Mode

ÖZ

OPTİK BİYO-TESPİT UYGULAMALARI AMACIYLA TASARLANMIŞ TEK BOYUTLU YARIK MODLU FOTONİK KRİSTAL KAVİTE

Erdil, Mertcan
Yüksek Lisans, Elektrik ve Elektronik Mühendisliği
Tez Yöneticisi: Doç. Dr. Serdar Kocaman

Temmuz 2020, 82 sayfa

Bu çalışmada, dönüştürücü eleman olarak tek boyutlu yarık modlu fotonik kristal kaviteleri kullanan kırıcılık indisi dayanaklı bir optik biyosensör sunduk. Yarık modlu tek boyutlu fotonik kristal kavitelerin ışığı düşük indisli bölgelerde çok küçük alanlara güçlü bir şekilde sıkıştırabilmelerinden kaynaklanan optik biyo-tespit uygulamalarına olan elverişliliklerinden faydalandık. Tasarım için gerekli teoriyi tanımladık ve cihaz performansını karakterize etmek için gerekli olan nümerik analizleri paylaştık. Ayrıca, bu tezde, rezonant kavitenin kalite faktörünü ve hassasiyetini birlikte artırabilen, optomekanik geri besleme döngüsüne dayanan performans geliştirici bir yöntem önerdik. Geliştirici mekanizma hedef analit ortama nüfuz ettiğinde tetiklenir ve kavite içerisinde üretilen enine optik gradyan kuvvetlerden faydalanarak kavite yarık genişliğini değiştirir. Optomekanik geri besleme döngüsü sayesinde, kalite faktörü ve hassasiyet arasındaki ödünleşim saf dışı bırakılabilir ve toplam başarı katsayısı artırılabilir. Tez boyunca, geliştirme yönteminin çalışma mekanizmasını, geliştirme düzeyini belirlemek için gerekli olan nümerik analizlerlerle birlikte gösterdik. Optomekanik performans geliştirme yöntemimiz kaviteyi etkilemeyecek bir şekilde herhangi bir rezonant yapıya

eklenebilir ve bu özelliği sayesinde diğer çeşitli sensör yapılarına uygulanma potansiyelini içinde barındırmaktadır.

Anahtar Kelimeler: Fotonik Kristal Kavite, Kırıcılık İndisi Tespiti, Optomekanik Geliştirme, Yarık Modu

To My Family

ACKNOWLEDGMENTS

I would like to start by expressing my deepest gratitude to my advisor, Prof. Serdar Kocaman. Without his assistance and guidance, it would not be possible to complete this study. He has always been an academic role model for me, and helped me a lot draw my career path. Apart from that, whether it is academic or not, he has always attended my problems like his own. I cannot describe how glad I am to have the chance to work with him during my undergraduate and graduate studies.

I also wish to thank Prof. Gönül Turhan Sayan, Prof. Haluk Külah, Prof. Hamza Kurt and Prof. Emre Yüce for accepting to take part in my thesis committee.

I would like to extend my sincere thanks to all my friends in our research group. I am indebted to Yigit Özer for his help on the optomechanical analysis of the nanobeams. I am also grateful to Alperen Gövdeli, Cem Kılıç, and Ulaş Topçuoğlu for fruitful discussions and enjoyable research environment. Finally, even if he is not a member of our group, many thanks to Cem Şahiner for his joyful contributions to the harmony of our working environment.

I would also like to thank my family for their support and love. They are always eager to do what it takes to promote my education and academic career. Especially, I am grateful to my grandfather for instilling an analytic way of thinking in me, which has helped me a lot during my academic journey. Finally, I would like to describe my sincerest appreciation to my wife, Gözde, for the love and understanding she shows. She has always stood by me during my studies. Her support and encouragement are precious to me.

During this study, I acknowledge the financial support of TUBITAK BIDEB 2210-A 2018/1 Scholarship Program.

TABLE OF CONTENTS

ABSTRACT v

ÖZ vii

ACKNOWLEDGMENTS x

LIST OF TABLES xiv

LIST OF FIGURES xv

LIST OF ABBREVIATIONS xviii

LIST OF SYMBOLS xix

CHAPTERS

1 INTRODUCTION 1

1.1 Optical Bio-sensing 1

1.2 Refractive Index Based Optical Bio-sensing 3

1.3 Research Focus and Thesis Organization 4

2 THEORETICAL BACKGROUND 7

2.1 Fundamentals of Electromagnetics 7

2.1.1 Maxwell's Equations 7

2.1.2 Wave Equation 8

2.1.3 Snell's Law and Total Internal Reflection 10

2.2 Photonic Crystals 12

2.2.1 Modes of a Photonic Crystal 12

2.2.2 Photonic Band Diagram 13

2.2.3 Practical PhC Configurations 16

2.2.3.1 1D PhC Nanobeams 17

2.2.3.2 2D PhC Slabs 18
2.3 Optical Forces 19
2.3.1 Types of Optical Forces 19
2.3.2 Transverse Optical Gradient Forces in Two Coupled Straight Waveguides 20
2.3.3 Cavity Optomechanics 22
3 HIGH Q-FACTOR 1D SLOT MODE PHOTONIC CRYSTAL NANOBEAM CAVITY 27
3.1 1D slot mode PhC Nanobeam Cavity 27
3.2 Figures of Merit 28
3.2.1 Q-factor (Q) 28
3.2.2 Sensitivity (S) 29
3.2.3 Mode Volume (V_m) 29
3.3 Cavity Design Procedure 30
3.4 Results and Numerical Analyses 33
3.4.1 Band Diagram Simulations 33
3.4.2 Mode Analysis and FDTD Simulations 39
4 SENSITIVITY ENHANCEMENT VIA OPTOMECHANICALLY INDUCED OPTICAL FEEDBACK 45
4.1 Q-factor vs Sensitivity Trade-Off 45
4.2 Operation Principle and the Optomechanical Feedback 47
4.3 Numerical Analyses and Results 50
4.3.1 Optical Force Calculations 50
4.3.2 Pump Signal Interference 51
4.3.3 Optomechanical Deflection 52

4.3.4 Sensitivity Enhancement 55
4.3.5 Q-factor Enhancement 60
5 CONCLUSION AND FUTURE WORK 65
REFERENCES 67
A. Photonic Band Diagram Extraction 77
B. Resonant Mode Analysis 79
C. Transmission Spectrum Analysis 81

LIST OF TABLES

TABLES

Table 3.1 Specified Design Parameters of the Cavity 38
Table 3.2 Cavity Performance as a Bio-sensor 43
Table 4.1 Resonant wavelength characteristics for various n_b and s values 55
Table 4.2 Sensitivity data for 10 nm and 20 nm deflection..... 57
Table 4.3 Resonant wavelength characteristics of a cavity with an initial slot width of 100 nm for various n_b and s values 58
Table 4.4 Sensitivity data of the cavity with the initial slot width of 100 nm for 10 nm and 20 nm deflection. 59
Table 4.5 Q-factor characteristics of the cavity for different n_b and s values 60
Table 4.6 Q-factor characteristics of the cavity for different n_b and s values. 62

LIST OF FIGURES

FIGURES

Figure 2.1. Demonstration of the light propagation from one medium to another. 10
Figure 2.2 Presentation of light guiding via total internal reflection. **(a)** In the absence of TIR, light travels to outer medium and cannot be guided. **(b)** In the presence of TIR, light can be guided through the medium with higher refractive index..... 11
Figure 2.3 Visual description of the periodical dielectric constant. **(a)** One dimensional, **(b)** two dimensional, and **(c)** three dimensional PhC configurations. 12
Figure 2.4 1D PhC photonic band diagram analysis. **(a)** Schematic of the 1D PhC, constructed by periodical placement of infinitely large plates. **(b)** Photonic band diagram of 1D PhC for TE polarization..... 14
Figure 2.5 2D PhC photonic band diagram analysis. **(a)** Schematic of 2D PhC square lattice formation. **(b)** Corresponding band diagram of the crystal..... 16
Figure 2.6 1D PhC nanobeam investigation. **(a)** Schematic of a 1D PhC nanobeam. **(b)**. Corresponding photonic band diagram. 17
Figure 2.7 2D PhC slab band diagram analysis. **(a)** Representative schematic of the device geometry. **(b)** Corresponding band diagram..... 19
Figure 2.8 Transverse optical force mechanics in two coupled straight waveguide system. **(a)** The schematic of a coupled two straight waveguide system. **(b)** Symmetric mode for E_z polarization at a wavelength of 1550 nm. **(c)** Anti-symmetric mode for E_z polarization at a wavelength of 1550 nm. 21
Figure 2.9 The representative schematic of a mechanically compliant Fabry-Pérot cavity. 23
Figure 3.1 1D PhC nanobeam cavity. **(a)** Schematics of the structure. L is the cavity length, w is the beam width, t is the thickness and a is the lattice periodicity. **(b)** Field enhancement inside the cavity. **(c)** Representative Lorentzian resonance..... 27
Figure 3.2 Unit cell design process. **(a)** The x-y cross-section of the unit cell. **(b)** y-z cross-section of the unit cell. **(c)** The band diagram of the unit cell with the initial parameters. 34

Figure 3.3 The characteristics of band edge frequencies with respect to the lattice constant. 35
Figure 3.4 The variation of band edge frequencies with respect to the nanobeam width. 36
Figure 3.5 The behavior of band edge frequencies with respect to the hole radius. 36
Figure 3.6 The effect of the slot width on the band edge frequencies. 37
Figure 3.7 Mirror strength with respect to the hole radius. 38
Figure 3.8 The band diagram of the center and end mirror segments. The dark red lines indicate the dielectric bands, while the dark blue lines depict the air bands. The dashed and the continuous lines represent the bands of the center and end mirror segments, respectively. 39
Figure 3.9 FDTD analysis of the designed cavity. **(a)** The refractive index distribution of the simulation environment. **(b)** The E_y mode profile of the fundamental resonance of the cavity. Inset: Zoom-in to the cavity center. 40
Figure 3.10 The slice of the cavity mode profile through the propagation direction and Gaussian-like fitting. The grey thick line depicts the field data, while the dotted red line indicates the Gaussian-like fitting. 41
Figure 3.11 FDTD analysis of simplified cavity. **(a)** The schematic of the simplified configuration. **(b)** Mode profile in the x-y plane. **(c)** Mode profile in the x-z plane. 42
Figure 3.12 The variation of resonance wavelength with respect to the background refractive index. 43
Figure 3.13 Transmission spectrum of the simplified cavity. 44
Figure 4.1 The trade-off between the sensitivity and Q-factor of the cavity with respect to the slot width. 46
Figure 4.2 **(a)** Isometric view of the device with the feedback loop. **(b)** Top view of the optomechanically enhanced bio-sensor. 48
Figure 4.3 The block diagram representation of the device operation and the performance enhancement feedback loop. 49

Figure 4.4 Optomechanical analysis. **(a)** The variation of the effective refractive index with respect to the slot width for different background refractive indices. **(b)** The normalized transverse optical gradient force with respect to the slot width for different background refractive indices. 51
Figure 4.5 The demonstration of the pump interference at the device output. The combined intensity at the output is presented for different background refractive index values. 52
Figure 4.6 Iterative optomechanical deflection analysis of the cavity with 11.3 μm slot waveguides appended at both sides. Red and blue lines present the deflection profile of the sides of the nanobeam and the iteration lines get darker with the increasing iteration number. **(a)** 20 nm total deflection of the nanobeam sides. **(b)** 10 nm total deflection of the nanobeam sides. 54
Figure 4.7 The presentation of the sensitivity enhancement for **(a)** 10 nm **(b)** 20 nm beam deflection. 56
Figure 4.8 The presentation of the sensitivity enhancement of the cavity with an initial slot width of 100 nm for **(a)** 10 nm **(b)** 20 nm beam deflection. 59
Figure 4.9 The presentation of the Q-factor enhancement of the cavity with an initial slot width of 50 nm for **(a)** 10 nm **(b)** 20 nm beam deflection. 61
Figure 4.10 The presentation of the Q-factor enhancement of the cavity with an initial slot width of 100 nm for **(a)** 10 nm **(b)** 20 nm beam deflection. 63

LIST OF ABBREVIATIONS

ABBREVIATIONS

CMOS:	Complementary Metal Oxide Semiconductor
FDTD:	Finite Difference Time Domain
FEM:	Finite Element Method
FWHM:	Full Width Half Maximum
MEEP:	MIT Electromagnetic Equation Propagation
MPB:	MIT Photonics Bands
PhC:	Photonic Crystal
RIU:	Refractive Index Unit
SOI:	Silicon-On-Insulator
SPR:	Surface Plasmon Resonance
TE:	Transverse Electric
TIR:	Total Internal Reflection
TM:	Transverse Magnetic
WGM:	Whispering Gallery Mode
1D:	One Dimensional
2D:	Two Dimensional
3D:	Three Dimensional

LIST OF SYMBOLS

SYMBOLS

a: Lattice Constant

$\boldsymbol{B}$: Magnetic Flux Density Vector

$\boldsymbol{b}$: Reciprocal Lattice Vector

c: Speed of light in free space

$\boldsymbol{D}$: Electric Displacement Vector

$\boldsymbol{E}$: Electric Field Intensity Vector

f_{res}: Optical Resonance Frequency

g_{OM}: Optomechanical Coupling Constant

$\boldsymbol{H}$: Magnetic Field Intensity Vector

$\hbar$: Planck's constant

$\boldsymbol{J}$: Current Density Vector

$\boldsymbol{k}$: Optical Wave Vector

n: Refractive Index

n_{eff}: Effective Refractive Index

P: Optical Power

Q: Quality Factor

$\boldsymbol{R}$: Lattice Vector

S: Sensitivity

Si: Silicon

V_m: Mode Volume

γ: Mirror Strength

ε: Dielectric Permittivity

ε_r: Relative Dielectric Permittivity

θ_c: Critical Angle

μ: Magnetic Permeability

ρ: Volume Charge Density

ω: Optical Angular Frequency

CHAPTER 1

INTRODUCTION

1.1 Optical Bio-sensing

Optical bio-sensing is the methodology of the detection of biological target analytes by utilizing the light as a sensing element [1]. Optical approach on bio-sensing brings a lot of advantages with itself when compared to its counterparts [2]–[4]. High speed, high sensitivity, and small footprint sensing mechanisms can be readily realized owing to the unique properties of photons [5]–[8]. With the help of wavelength division multiplexing configurations, the multi-channel optical data can be transmitted and processed through a single optical link, enhancing the bandwidth of the operation and facilitating the implementation of optical sensor arrays [9]. Furthermore, optical bio-sensing structures are resilient to electromagnetic interference, unlike their electronic complements. With the rapid developments in the optical device fabrication technology, the amount of advanced, top-quality optical bio-sensors in the market is expected to increase [4], [10], [11].

There are variety of application areas, where the optical bio-sensors are widely used, ranging from clinical process and environmental monitoring to bio-warfare control [1], [2], [12]–[18]. From the biomedical perspective, the optical bio-sensors undertake a significant role in terms of the detection of lots of essential particles such as proteins, monoecellular livings, nucleic acids, and many other single nanoparticles. There are many fatal diseases, in which the early diagnosis is crucial for the successful treatment of the patients. Most of the time, these diseases manifest themselves in the patient's blood and tissues, and the optical bio-sensors have a

strong potential to detect their indicators. In addition, they are highly useful in drug detection and delivery [19].

In its simplest form, an optical bio-sensor is usually composed of a receptor and a transduction part. The receptor is utilized to select the target analyte in a mixed environment, while the transduction mechanism is the part converting the interaction between the bio-receptor and the target analyte to an optical signal, which can be detected by the photodetection schemes at the output [1]. The way of interaction between the sensing layer and the target analyte affects the output of the transducer uniquely, resulting in the characterization of the particle of interest.

There are diverse methods in order to implement an optical bio-sensor [2], [9], [16], [20]–[23]. Among them, one typical method is to use optrodes. The optrode is a type of optical electrodes, implemented by utilizing fiber optic cables [24]. A fiber optic cable is a component, used for the transmission of light through long distances with minimum loss, and it can be visualized as an optical pipe [25]. The light propagates through the fiber optic cable, and it is focused on a sensing layer at the fiber output [24]. When the analyte interacts with the sensing layer, the output of the fiber is modified due to the altered optical characteristics of the sensing layer. The way of interaction may differ with respect to the sensing layer properties. Flourescence and chemoilluminescence are among the popular phenomena used in bio-optrodes. There are also applications where the evanescent fields of the fiber modes are utilized for optical bio-sensing purposes. In this method, the evanescently coupled field at the fiber cladding excites the materials/particles interacting with the target analyte. In addition to the fibers, optical planar waveguides are also utilized for optical bio-sensing [24]. The planar waveguides are the rectangular structures functioning like optical fibers, however, they perform on-chip light transmission and guiding rather than long distances [26].

1.2 Refractive Index Based Optical Bio-sensing

Another way of optical bio-sensing is to benefit from the change of the refractive index of the background medium due to the presence of the target analyte. Such an application has one strong advantage over other types of optical bio-detection: Label-free sensing [27]–[30]. Refractive index based optical bio-sensing offers label-free sensing, meaning that the sensing operation does not require any specific interface material, which is supposed to interact with the target analyte in order to be detected. Such an advantage enables the implementation of real-time, non-complex monitoring of the target materials.

The response of the sensor to the variations in the background refractive index is, obviously, correlated with the interaction strength between the target analyte and the photons; thus, resonant structures are naturally preferred for this purpose [31]. As the resonant structures strongly localize the light both in time and spatial domain, they become the prominent assets of the label-free sensing applications. Many diverse resonant structures are already utilized for label-free optical bio-detection purposes, and lots of remarkable studies are already present in the literature. Fabry-Pérot cavities, WGM structures, micro-rings, and photonic crystal (PhC) cavities are among the most preferred resonant components used for optical bio-sensing purposes [32]–[39]. Apart from them, making use of surface plasmon resonance (SPR) is highly popular, so far [22], [30]. PhC cavity structures also step forward when compared to the other types of resonant components, as they allow the realization of highly sensitive, ultra-small devices while offering simple integration and compatibility with complementary metal oxide semiconductor (CMOS) fabrication technology [40]. Especially, one dimensional (1D) PhC nanobeam cavities can localize the light much more strongly, owing to their compact device geometry. By this way, they are highly suitable for large-scale, extended sensing operations [31], [38], [41].

1.3 Research Focus and Thesis Organization

In this study, an optically resonant structure is designed and its potential to be utilized in refractive index based optical bio-sensing applications is examined. Throughout the thesis, more focus is placed on the characterization of the optical transduction of the information of background refractive index variations. An optomechanical performance enhancement method is applied to the structure and its effect on the efficiency of transduction is quantified via various numerical analyses. The enhancement of the device is realized by benefiting from the transverse optical gradient forces inside the structure. An interference mechanism controlling the amount of force inside the device is implemented in order to enhance the device performance. The focus of the research can be grouped into two main categories, namely the design of the 1D PhC nanobeam cavity and the optomechanical enhancement of the device performance. Finally, the research points out the elimination of the intrinsic trade-off between the two different performance factors, realized by the help of the optical positive feedback generated by the optomechanical enhancement setup.

The organization of the remaining parts of the thesis is as follows. In Chapter 2, a detailed theoretical background is provided in order to assist the reader who does not have sufficient knowledge of the field. The theoretical background starts from the fundamental Maxwell's Equations and elaborates on the various concepts frequently used in the analysis of PhC structures. Moreover, it informs the reader with the fundamentals of the PhC configurations and the basics of the optomechanics. In Chapter 3, the design of the 1D PhC cavity bio-sensor is presented in detail. The steps followed during the design process are extended, and the figures of merit considered during the design are shared together with the results of the numerical analyses. In Chapter 4, the enhancement of the device performance by the optomechanical feedback loop is characterized, and the corresponding numerical findings are given in detail. The effects of several parameters on the enhancement performance are also investigated. Finally, in Chapter 5, a conclusion has been made

on the potential usage of the enhancement method applied to the 1D PhC nanobeam cavity. The experimental feasibility is also discussed, and the future pathway of the study is drawn.

CHAPTER 2

THEORETICAL BACKGROUND

The second chapter presents a general overview of the theoretical background of the study in order to enable the reader to comprehend the emphasis of the thesis comfortably. Helpful information on the fundamentals of electromagnetics, PhCs, and optomechanics can be found.

2.1 Fundamentals of Electromagnetics

In its simplest form, electromagnetics is a discipline investigating the relationship and interaction between the electrical charges in a given medium. It also covers the behavior of the electromagnetic waves propagating in a certain medium [42]. As the light itself is an electromagnetic wave, an introduction to the basics of the electromagnetic theory will be quite useful for the readers lacking sufficient background.

2.1.1 Maxwell's Equations

The characteristics of an electromagnetic wave in a given medium can be described by the equations derived by James C. Maxwell. These equations can be presented in four main differential equations [43], as given in Equation 2.1 to Equation 2.4.

$$\boldsymbol{\nabla} \, x \, \boldsymbol{H} = \frac{d\boldsymbol{D}}{dt} + \boldsymbol{J} \tag{2.1}$$

$$\boldsymbol{\nabla} \, x \, \boldsymbol{E} = -\frac{d\boldsymbol{B}}{dt} \tag{2.2}$$

$$\boldsymbol{\nabla}.\boldsymbol{D} = \rho \tag{2.3}$$

$$\boldsymbol{\nabla}.\boldsymbol{B} = 0 \tag{2.4}$$

Through Equation 2.1 and Equation 2.4, $\boldsymbol{E}$ and $\boldsymbol{H}$ are the electric and magnetic field intensities, respectively, whereas $\boldsymbol{D}$ and $\boldsymbol{B}$ are the electric displacement vector and magnetic flux density. Finally, $\boldsymbol{J}$ is the current density, and ρ is the volume charge density.

2.1.2 Wave Equation

The wave equation is the main differential equation that helps us analyze the characteristics of an electromagnetic wave in a given medium, and it can be derived by utilizing Maxwell's equations. In the optical frequency range, most of the materials of interest are non-magnetic, moreover, throughout this study, we will be dealing with source-free media. Therefore, it is reasonable to present these equations in a suitable way for our application purpose [26].

$$\boldsymbol{\nabla}\, x\, \boldsymbol{H} = \frac{\partial \boldsymbol{D}}{\partial t} \tag{2.5}$$

$$\boldsymbol{\nabla}\, x\, \boldsymbol{E} = -\frac{\partial \boldsymbol{B}}{\partial t} \tag{2.6}$$

$$\boldsymbol{\nabla}.\boldsymbol{D} = 0 \tag{2.7}$$

$$\boldsymbol{\nabla}.\boldsymbol{B} = 0 \tag{2.8}$$

From Equation 2.5 to Equation 2.7, the modified versions of Maxwell's equations are given to be utilized for non-magnetic, source-free media. In order to obtain a decoupled equation by using Maxwell's equations, we can start by taking the curls of both sides in Equation 2.6. Before initiating the derivation, we can make some assumptions for further simplification. To begin with, we can assume a linear and isotropic medium, where the dielectric permittivity (ε) and the magnetic permeability

(μ) are independent of the field amplitudes. In such a case, we obtain the expression given in Equation 2.9.

$$\boldsymbol{\nabla}\, x\, (\boldsymbol{\nabla}\, x\, \boldsymbol{E}) = \boldsymbol{\nabla}\, x \left(-\frac{\partial \mu \boldsymbol{H}}{\partial t}\right) \tag{2.9}$$

Due to the non-magnetic behavior of materials in the optical frequency range, the magnetic permeability can be treated as it is independent of both time and position; and we can obtain the following expression.

$$\boldsymbol{\nabla}\, x\, (\boldsymbol{\nabla}\, x\, \boldsymbol{E}) = -\mu \frac{\partial}{\partial t} (\boldsymbol{\nabla}\, x\, \boldsymbol{H}) \tag{2.10}$$

By substituting Equation 2.5 into Equation 2.10, and considering a stationary medium in the time domain, we can obtain the expression given in Equation 2.11.

$$\boldsymbol{\nabla}\, x\, (\boldsymbol{\nabla}\, x\, \boldsymbol{E}) = -\mu \frac{\partial}{\partial t} \left(\frac{\partial \boldsymbol{D}}{\partial t}\right) = -\mu\varepsilon \frac{\partial^2 \boldsymbol{E}}{\partial t^2} \tag{2.11}$$

In Equation 2.11, a decoupled differential equation with $\boldsymbol{E}$ as a variable is obtained. The expression on the left-hand side of Equation 2.11 can be simplified via the vector identity in Equation 2.12.

$$\boldsymbol{\nabla}\, x\, (\boldsymbol{\nabla}\, x\, \boldsymbol{E}) = \boldsymbol{\nabla}\, (\boldsymbol{\nabla}\, .\boldsymbol{E}) - \boldsymbol{\nabla}^2\, .\, \boldsymbol{E} \tag{2.12}$$

Applying the identity in Equation 2.12, we can obtain the form in Equation 2.13.

$$\boldsymbol{\nabla}^2\, .\, \boldsymbol{E} - \mu\varepsilon \frac{\partial^2 \boldsymbol{E}}{\partial t^2} = \nabla\, (\boldsymbol{\nabla}\, .\boldsymbol{E}) \tag{2.13}$$

Note that in Equation 2.13, the expression on the right-hand side is negligibly smaller, and consequently, the homogenous part of the equation interests us more. Therefore, the final expression of the wave equation is given in Equation 2.14.

$$\boldsymbol{\nabla}^2\, .\, \boldsymbol{E} - \mu\varepsilon \frac{\partial^2 \boldsymbol{E}}{\partial t^2} = 0 \tag{2.14}$$

2.1.3 Snell's Law and Total Internal Reflection

Another important relationship for understanding light behavior is Snell's Law, which investigates the propagation of an electromagnetic wave from one medium to another. Consider an environment, consisting of two different media with different refractive indices (n), as in Figure 2.1.

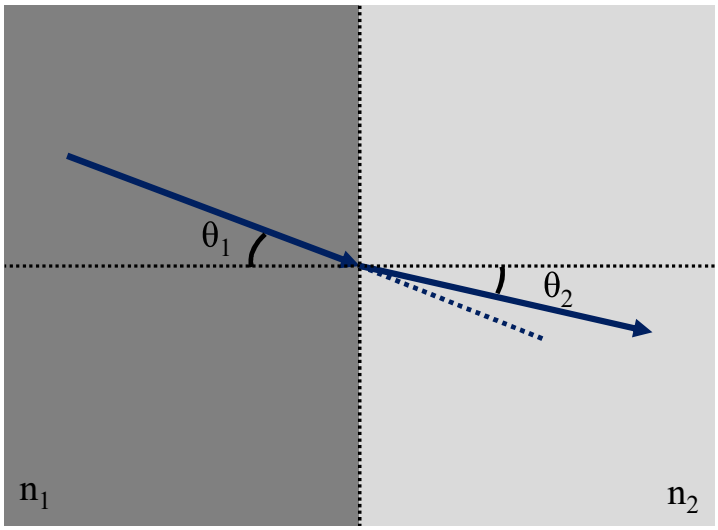

Figure 2.1. Demonstration of the light propagation from one medium to another.

As it can be seen in Figure 2.1, light incident on the boundary between two media gets refracted. The modeling of light refraction is given by Snell's Law, provided in Equation 2.15 [26].

$$n_1 \sin\theta_1 = n_2 \sin\theta_2 \tag{2.15}$$

In Equation 2.15, n_1 and n_2 depict the refractive indices of the first and second media, respectively, whereas θ_1 and θ_2 are the angles between the boundary normal and the propagation direction of the light in medium 1 and 2, respectively. Observing Snell's Law gives an insight into the bending of light when traveling from one medium to another. Further investigation of the formula can reveal significant consequences. By examining Equation 2.15, one can notice that as θ_1 increases, θ_2 also gets larger. For the case where n_1 is greater than n_2, after some point, increasing the incident

angle forces the sinusoidal term on the right-hand side of Equation 2.15 to be larger than 1, creating a scenario with no physical interpretation. Therefore, after a certain incident angle value, the light is not allowed to travel to the medium, and it is reflected back at the boundary. This phenomenon is called the total internal reflection (TIR), and the minimum value of the incident angle resulting in the total internal reflection is called the critical angle (θ_c), given in Equation 2.16 [42].

$$\theta_c = \sin^{-1}(\frac{n_2}{n_1}) \tag{2.16}$$

The total internal reflection is one of the most important principles for the integrated photonics. It constitutes the building block of the wave guiding and manipulation in many configurations. Guiding of light via total internal reflection can be better understood in Figure 2.2.

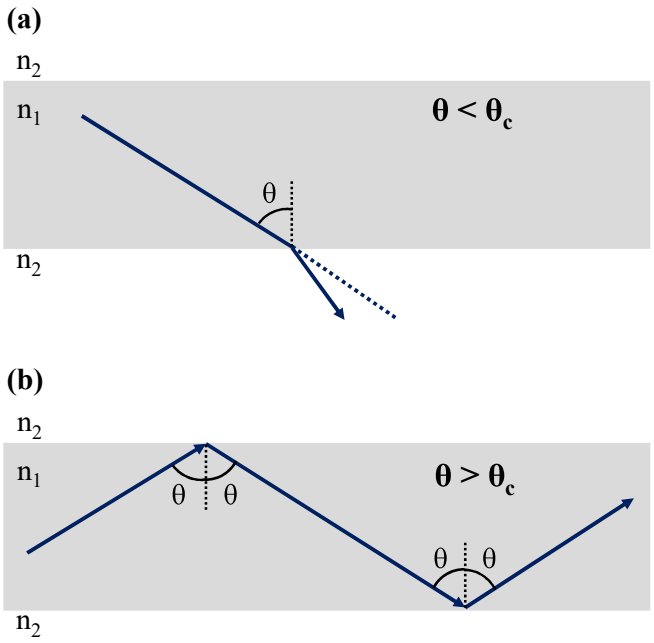

Figure 2.2 Presentation of light guiding via total internal reflection. **(a)** In the absence of TIR, light travels to outer medium and cannot be guided. **(b)** In the presence of TIR, light can be guided through the medium with higher refractive index.

2.2 Photonic Crystals

A photonic crystal (PhC) is an artificial material, constructed by the periodical placement of the dielectric constant. Owing to their periodic configuration, PhCs possess bandgaps, preventing the propagation of photons with certain energies [44]. Such a characteristic is highly analogous to the semiconductor physics in solid-state theory, and it allows us to confine and manipulate the light inside the PhCs. Since their first proposal by Yablonovitch and John [45], [46], these structures are highly preferred in diverse areas with various application purposes [47]–[49]. A visual presentation of different types of PhCs can be seen in Figure 2.3.

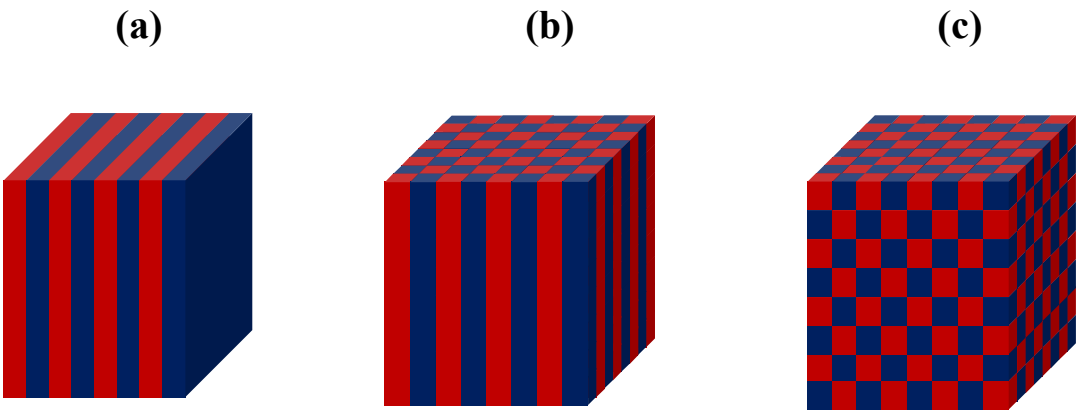

Figure 2.3 Visual description of the periodical dielectric constant. **(a)** One dimensional, **(b)** two dimensional, and **(c)** three dimensional PhC configurations.

As shown in Figure 2.3, PhCs can be implemented by applying the dielectric periodicity in one, two, and three dimensions.

2.2.1 Modes of a Photonic Crystal

The modes allowed to propagate through PhCs are the solutions of the wave equation. In order to analyze these modes, first, let us extend the fields into their spatial harmonics and get rid of the time dependence as in Equation 2.17 and Equation 2.18 [43].

$$\boldsymbol{H}(\boldsymbol{r},t) = \boldsymbol{H}(\boldsymbol{r})e^{-i\omega t} \tag{2.17}$$

$$\boldsymbol{E}(\boldsymbol{r},t) = \boldsymbol{E}(\boldsymbol{r})e^{-i\omega t} \tag{2.18}$$

When this is the case, the wave equation for the magnetic field can be rearranged, as given in Equation 2.19.

$$\boldsymbol{\nabla}\, x \left(\frac{1}{\varepsilon_r(\boldsymbol{r})} \boldsymbol{\nabla}\, x\, \boldsymbol{H}(\boldsymbol{r}) \right) = \left(\frac{\omega}{c}\right)^2 \boldsymbol{H}(\boldsymbol{r}) \tag{2.19}$$

In Equation 2.19, $\boldsymbol{r}$, ε_r, ω, and c are the position vector, relative dielectric permittivity function, angular optical frequency, and the speed of light in free space, respectively. Notice that the above equation can be rewritten as an eigenvalue problem.

$$\hat{\Psi}\boldsymbol{H}(\boldsymbol{r}) = \left(\frac{\omega}{c}\right)^2 \boldsymbol{H}(\boldsymbol{r}) \tag{2.20}$$

In such a problem, the modes of the photonic crystals become the eigenfunctions with the eigenvalues of $(\omega/c)^2$. One important notice is that the operator, Ψ, is a Hermitian operator. There are several important remarks for the eigenfunctions of Hermitian operators:

- Hermitian operators are linear: If $\boldsymbol{H_1(r)}$ and $\boldsymbol{H_2(r)}$ are the eigenfunctions of Ψ, $k_1\boldsymbol{H_1(r)} + k_2\boldsymbol{H_2(r)}$ is also an eigenfunction.
- The eigenfunctions of Hermitian operators have real eigenvalues.
- The eigenfunctions of Hermitian operators are orthogonal to each other.

These properties are crucial for gaining insight into the modes of PhCs. However, more detailed information about the modes of PhCs can be obtained via the band diagram analysis.

2.2.2 Photonic Band Diagram

The photonic band diagram of a PhC incorporates the information about the dispersion relation inside the crystal. The design process of a PhC can be conducted

through the band diagram analysis. The photonic band diagram can be extracted analytically or numerically via different methods, including plane wave expansion, etc. [50].

Consider the one dimensional (1D) PhC given in Figure 2.4(a). Infinitely wide dielectric planes are placed periodically, with air in between them. The structure exhibits a discrete translational symmetry along one direction, and the position of any plate can be expressed in terms of the lattice vector (***R***) given in Equation 2.21 [43].

$$\boldsymbol{R} = c_1 a \boldsymbol{x} \tag{2.21}$$

In Equation 2.21, $\boldsymbol{x}$ is the unit vector in x-direction, while c_1 is an integer, and a is the lattice periodicity, i.e., the distance between the consecutive layers. For 1D configuration, the dispersion relation for the light with transverse-electric (TE) polarization is numerically analyzed via MIT Photonic Bands (MPB) software package [51] and given in Figure 2.4(b). The thickness of the plates is chosen as the $0.5a$. As one can see in the figure, there are two bands, indicating the allowable modes in the crystal. In addition to the bands, there is also a region where no modes exist for any value of k. This region is the photonic bandgap of the crystal, and in this region, light is not allowed to propagate through the structure.

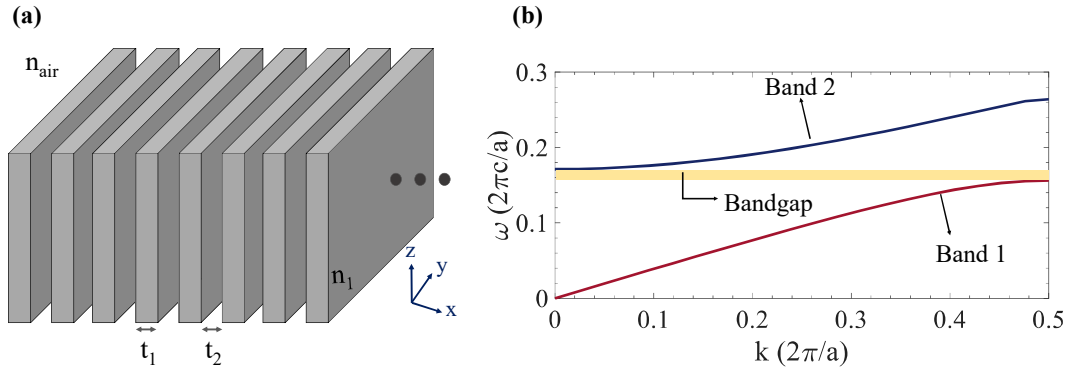

Figure 2.4 1D PhC photonic band diagram analysis. **(a)** Schematic of the 1D PhC, constructed by periodical placement of infinitely large plates. **(b)** Photonic band diagram of 1D PhC for TE polarization.

Note that the band diagram demonstrates the allowed energy states inside the crystal in *k*-space. The dispersion relation of the crystal is also periodic in *k*-space, in terms of the reciprocal lattice vector, as given in Equation 2.22 [43].

$$\boldsymbol{b} = c_2 \frac{2\pi}{a} \boldsymbol{x} \tag{2.22}$$

For the two dimensional (2D) configuration, we have a similar scenario. Observe the schematic of the 2D PhC, constructed by the periodical arrangement of infinite-height rods in a square lattice formation in Figure 2.5(a). Note that in this case, we have two symmetry axes, meaning that our lattice vector is a linear combination of two primitive lattice vectors, directed in primary axes.

$$\boldsymbol{R} = c_1 a_x \boldsymbol{x} + c_2 a_y \boldsymbol{y} \tag{2.23}$$

In Equation 2.23, a_x and a_y are the lattice periodicity along x and y directions, respectively. $\boldsymbol{x}$ and $\boldsymbol{y}$ represent the unit vectors, while $c_{1,2}$ are integers. Consequently, the reciprocal lattice vector can be expressed as in Equation 2.24.

$$\boldsymbol{b} = c_1 \frac{2\pi}{a_x} \boldsymbol{x} + c_2 \frac{2\pi}{a_y} \boldsymbol{y} \tag{2.24}$$

As a consequence of the discrete structural symmetry, we do not need to analyze the entire *k*-space. Analyzing only the region given as a blue triangle in Figure 2.5(a) will be sufficient, and this region is called the irreducible Brillouin zone [43]. Investigating the device behavior only in this region will give the necessary information to extract the entire characteristics. Moreover, since most of the interesting phenomena are exhibited at the boundary of this region, for 2D PhCs, considering only the edges of the irreducible Brillouin zone is usually sufficient. The band diagram of the 2D PhC with the design parameters of $a_x = a_y = a$ and $r = 0.1a$ is given with a rod refractive index of 3.48 in Figure 2.5(b) for transverse-magnetic (TM) polarization.

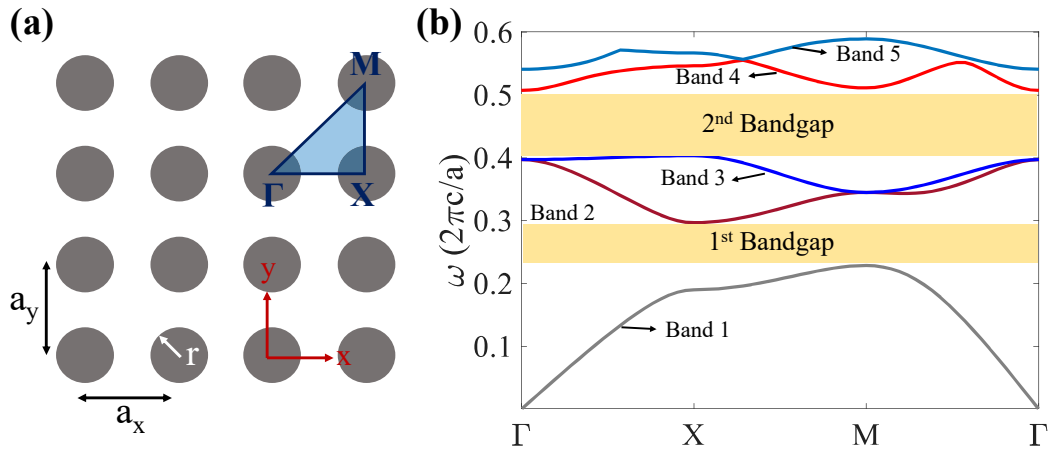

Figure 2.5 2D PhC photonic band diagram analysis. **(a)** Schematic of 2D PhC square lattice formation. **(b)** Corresponding band diagram of the crystal.

In Figure 2.5(b), two bandgaps between the first and second bands and between the third and fourth bands can be clearly seen. Engineering the design parameters such as the rod radius and lattice periodicity enables us to modify the size and position of the gap in accordance with the design purpose.

2.2.3 Practical PhC Configurations

So far, we have dealt with structures extending to infinity, at least in one dimension. Such structures are not practical, even though they are quite useful for the demonstration of the fundamentals. One can propose to implement a three dimensional (3D) PhC; however, implementation of 3D PhCs is highly challenging, considering the current micro-fabrication technology. As more practical alternatives, 1D PhC nanobeams or 2D PhC slabs can be utilized. In these configurations, through the direction where the periodicity is not present, the light is guided via index guiding [52], [53]. Therefore, these devices have finite sizes, and they are suitable from the perspective of fabrication feasibility.

2.2.3.1 1D PhC Nanobeams

1D PhC nanobeams are the periodical structures, constructed by the periodical placement of dielectric constant along the propagation direction [43]. While the light is guided by the Bloch modes in the direction of propagation, in the transverse regions, it is guided by total internal reflection. A 1D PhC nanobeam is given in Figure 2.6(a). The presented nanobeam is constructed by etching periodical air holes into a dielectric material along the direction of propagation. The way of introduction of the dielectric periodicity can vary. Many interesting designs with different features are already present in the literature [54]–[56].

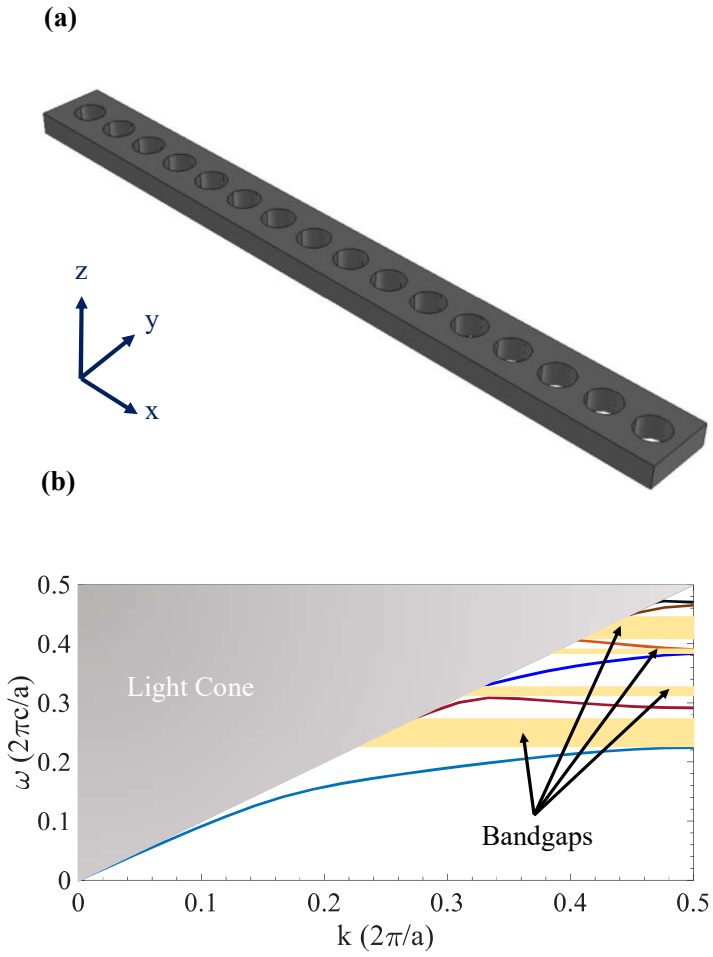

Figure 2.6 1D PhC nanobeam investigation. **(a)** Schematic of a 1D PhC nanobeam. **(b)**. Corresponding photonic band diagram.

The photonic band diagram of a 1D PhC nanobeam can be observed in Figure 2.6(b). As one can expect, it is quite similar to the band diagrams presented previously. However, for the PhC structures utilizing index guiding, we are only interested in the region where the structure is able to guide the light in the transverse directions, i.e., the region where the effective refractive index of the mode is larger than the maximum of the cladding refractive index. The modes not satisfying the condition cannot be guided through the structure and, eventually, they couple to the radiation modes in the air. In the photonic band diagram, the region encapsulating these modes are named as the light cone [43], and it can be observed in Figure 2.6(b) as a grey triangular area.

2.2.3.2 2D PhC Slabs

In addition to 1D PhC nanobeams, 2D PhC slabs are also utilized in practical configurations [57], [58]. In these structures, the light is guided by the finite discrete translational symmetry in two dimensions, while index guiding is used for the third dimension. In Figure 2.7(a), a 2D PhC slab configuration, implemented by etching periodical air holes into a dielectric slab in a square lattice formation, is presented. The band diagram of the 2D PhC slab is also quite similar to its reduced dimensional counterpart. Similar to the case of 1D nanobeam, the light cone is taken into consideration. A band diagram for a 2D PhC slab structure is illustrated in Figure 2.7(b).

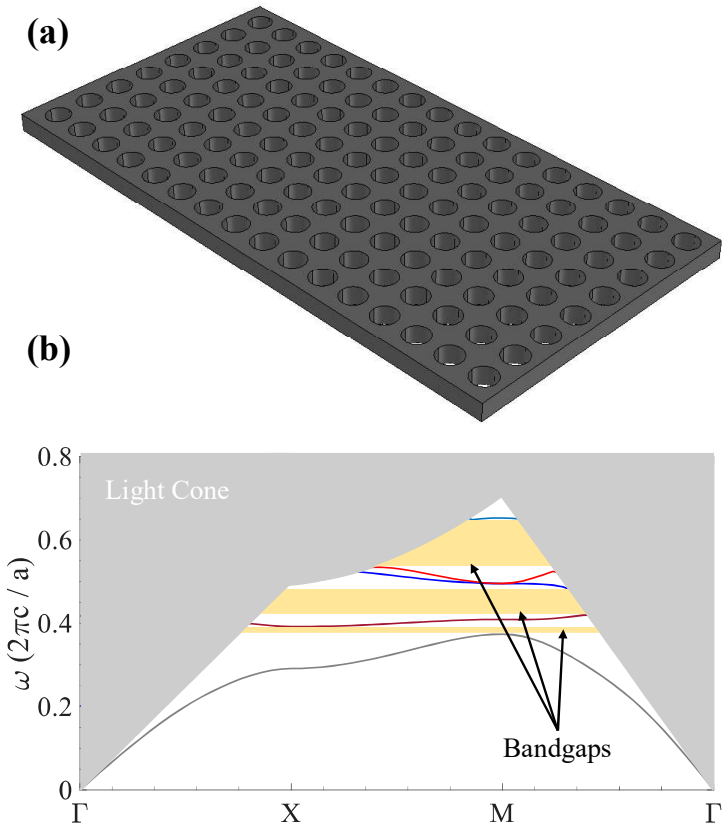

Figure 2.7 2D PhC slab band diagram analysis. **(a)** Representative schematic of the device geometry. **(b)** Corresponding band diagram.

2.3 Optical Forces

In this chapter, optical forces in the photonic structures are discussed. When light interacts with matters, it exerts a force on them [59]. Such a force is highly useful and can be utilized for the mechanical manipulation of light, giving birth to interesting applications [60]–[65].

2.3.1 Types of Optical Forces

The way of mechanical interaction between the light and the matter may vary. One type of optical force is the radiation pressure, where a force is applied to the material

as a consequence of the absorption, scattering, or radiation of the light [59]. The scattering forces, a branch of the radiation pressure forces, are one of the most commonly occurred force types. In this type, the force is exerted by the photon scattering, and the momenta of the photons are transferred to the material. When this is the case, the applied force is in the same direction as that of the light propagation [59], [60]. Moreover, the amount of applied force is proportional to the number of scattered photon; hence, the light intensity. Radiation pressure forces have a lot of important applications, including the optical traps, utilized to stabilize the small particles in an optomechanical way [66], [67].

The second type of optical force is called the gradient force. When the light propagates through a transparent material, it causes the electric dipoles to fluctuate [59]. The fluctuation results in a time-averaged optical force. The force is parallel to the direction of intensity gradient and also, the magnitude of the force scales with it.

In addition to the forces mentioned above, there are other types of optical forces, such as the optical binding forces, referring to the forces between the particles exposed to intense light [59], [68].

2.3.2 Transverse Optical Gradient Forces in Two Coupled Straight Waveguides

Consider the coupled two straight waveguides given in Figure 2.8(a). When these waveguides are sufficiently brought near to each other, they evanescently couple, and two modes appear as given in Figure 2.8(b)-(c) [69]. The two modes differ in the symmetry properties of the electric field component in the z-direction (E_z) as symmetric and anti-symmetric modes with respect to the $y = 0$ plane. Due to the evanescent coupling between them, strong transverse optical forces arouse between the waveguides, and the direction of the force is determined with respect to the phase difference of the light in the waveguides [69], [70]. Therefore, the force is attractive

for the symmetric mode, whereas the repulsive forces arouse for the anti-symmetric case.

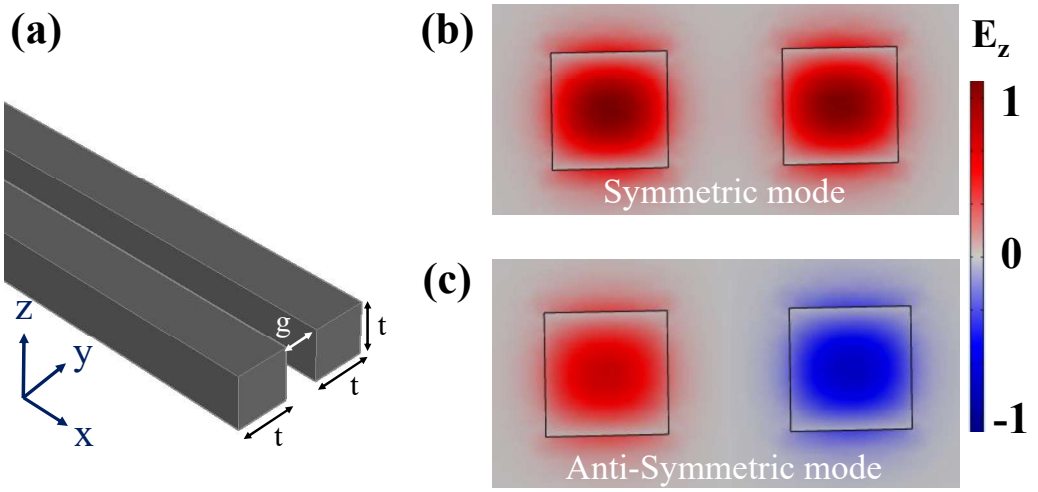

Figure 2.8 Transverse optical force mechanics in two coupled straight waveguide system. **(a)** The schematic of a coupled two straight waveguide system. **(b)** Symmetric mode for E_z polarization at a wavelength of 1550 nm. **(c)** Anti-symmetric mode for E_z polarization at a wavelength of 1550 nm.

The analysis of the transverse optical gradient forces can be realized via the Maxwell stress tensor formalism. However, the same analysis can be done by a method described by Povinelli et al. The energy injected to the coupled system can be expressed as in Equation 2.25 [69].

$$U = N\hbar\omega \tag{2.25}$$

In Equation 2.25, U is the total energy, N is the number of photons, $\hbar$ is the normalized Planck's constant, and ω is the optical angular frequency. In this case, the optical force due to the evanescent coupling can be written as in Equation 2.26.

$$F = -\frac{dU}{dg}\Big|_k = -\frac{d(N\hbar\omega)}{dg}\Big|_k \tag{2.26}$$

In Equation 2.26, F is the generated optical force, g is the separation between the waveguides, and k is the wave vector. Further simplification turns Equation 2.26 into the expression given in Equation 2.27.

$$F = -N\hbar \frac{d\omega}{dg}\Big|_{\boldsymbol{k}} = -\frac{1}{\omega}\frac{d\omega}{dg}\Big|_{\boldsymbol{k}} U \tag{2.27}$$

The expression in Equation 2.26 can be rearranged and delivered in terms of the effective refractive index (n_{eff}) of the coupled system [62].

$$\frac{F}{LP} = -\frac{1}{c}\frac{dn_{eff}}{dg} \tag{2.28}$$

In Equation 2.28, the L is the length of the waveguides, c is the speed of light in vacuum, and P is the power injected into the system. By observing Equation 2.28, it is evident that the force applied to the waveguides is proportional to the rate of change of the effective refractive index with respect to the separation between the waveguides.

Applied force creates a deflection on the waveguide boundaries, and the dynamics of the deflection ($u(x)$) can be examined via the Euler-Bernoulli beam theory, given in Equation 2.29 [62].

$$F = \frac{d^2u}{dx^2}\left(EI\frac{d^2u}{dx^2}\right) = E\frac{LAt^2}{12}\frac{d^4u}{dx^4} \tag{2.29}$$

In Equation 2.29, u is the amount of deflection, A is the cross-sectional area of the waveguide, t is the thickness, and E is Young's modulus.

2.3.3 Cavity Optomechanics

Cavity optomechanics is one of the most important areas where the optical forces are utilized. It mainly investigates the dynamics of mechanically compliant optical cavities. The optical properties of the cavity are coupled to the mechanical state of

the system, and the most basic form of such a system can be described as a Fabry-Pérot cavity with one fixed and one movable mirror. The representative configuration is visualized in Figure 2.9. When one of the mirrors is free, the resonance frequency of the cavity becomes a function of the mirror displacement, as in Equation 2.30 [63].

$$\omega_{res}^{(n)}(x) \cong \omega_{res}^{(n)}(0) - g_{OM}x \tag{2.30}$$

Where,

$$\omega_{res}^{(n)}(0) = \frac{cn\pi}{L} \tag{2.31}$$

In Equation 2.30 and Equation 2.31, ω_{res} is the angular optical resonance frequency, x is the position displacement of the mirror, and n is the integer, indicating the order of the resonance. g_{OM} is called as the optomechanical coupling constant and demonstrates the rate of change of the optical resonance frequency with respect to the displacement. Hence, in the case of the Fabry-Pérot cavity,

$$g_{OM} = \frac{d\omega_{res}^{(n)}}{dx} = \frac{\omega_{res}^{(n)}(0)}{L} \tag{2.32}$$

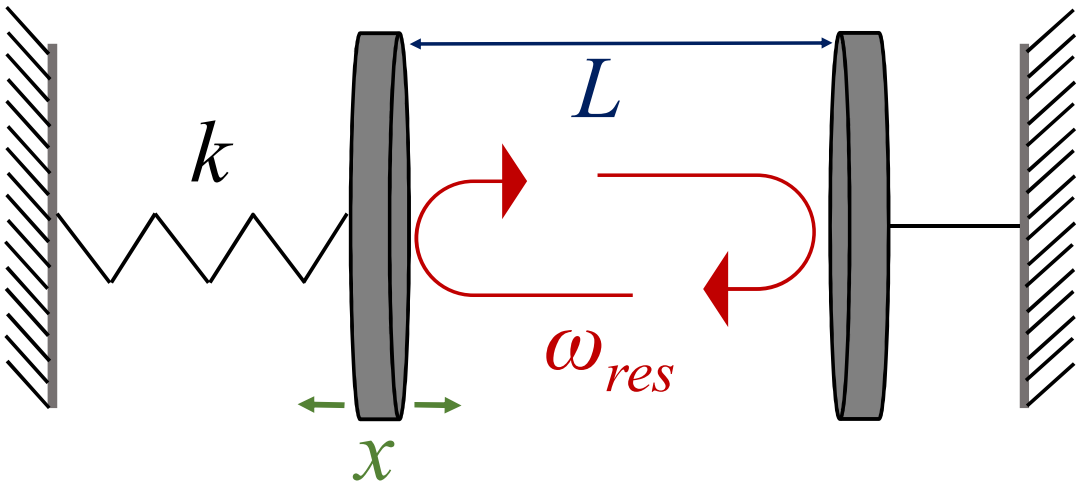

Figure 2.9 The representative schematic of a mechanically compliant Fabry-Pérot cavity.

In the system given in Figure 2.9, the photons inside the cavity transfer their momenta to the movable mirror, as they reflect from it. The change in the momentum of the mirror results in a change in its position. Similarly, any externally mechanical input to the system modifies the cavity resonance by changing the length of the cavity. Therefore, the optical and the mechanical system are coupled to each other, and the dynamics of the system are determined via the coupled equations of motion, provided in Equation 2.33 and Equation 2.34.

$$\frac{d\alpha}{dt} = -\frac{\kappa}{2}\alpha + i\,(\Delta + g_{OM}x)\alpha + \sqrt{\kappa_{ex}\alpha_{in}} \tag{2.33}$$

$$m_{eff}\frac{d^2x}{dt^2} = -m_{eff}\Omega_m^2 x - m_{eff}\Gamma_m\frac{dx}{dt} + \hbar g_{OM}|\alpha|^2 \tag{2.34}$$

In Equation 2.33 and Equation 2.34, α is the average photon amplitude inside the cavity, κ is the decay rate of the cavity, κ_{ex} is the external coupling loss rate of the optical input, Δ, given as $(\omega_L-\omega_{res})$, is the spectral difference between the laser frequency and cavity resonance, α_{in} is the amplitude of the laser input, m_{eff} is the effective mass of the mechanically compliant system, Ω_m is the angular mechanical resonance frequency, and Γ_m is the decay rate of the mechanical damping rate. By observing Equation 2.33 and Equation 2.34, the coupling between the optical and mechanical domains can be readily realized.

By manipulating the optomechanical coupling, lots of important phenomena are demonstrated in both the classical and the quantum regime. First of all, by modifying the photon amplitude inside the cavity, both the real and the imaginary parts of the eigenvalues of the mechanical system can be tuned. The change in the real part via optically results in a shift in the mechanical resonance frequency of the system, and it is called the *'optical spring effect'* [63], [71]. On the other hand, the imaginary part is associated with the mechanical loss, and the optical modification of it can create an optomechanical damping coefficient, which can be utilized to amplify or cool the mechanical modes. The amplification leads to the realization of highly narrow mechanical modes, i.e., the phonon lasing, while the cooling is highly desirable for

the high-precision displacement measurement near the standard quantum limit [63], [72]–[74].

CHAPTER 3

HIGH Q-FACTOR 1D SLOT MODE PHOTONIC CRYSTAL NANOBEAM CAVITY

The third chapter provides information about the design steps of 1D PhC nanobeam cavities. The figures of merit from the optical biosensing purposes are explained in detail. The designed cavity is numerically analyzed, and the results are presented.

3.1 1D slot mode PhC Nanobeam Cavity

1D PhC nanobeams are the periodical dielectric structures, where a dielectric permittivity contrast is present along the direction of propagation [43]. Introduced dielectric periodicity creates a bandgap, a spectral region in which the light cannot propagate through the nanobeam. A cavity can be created inside the nanobeam by disturbing the discrete translational symmetry via introduced defects, impurities, etc [12], [55]. In Figure 3.1(a), a representative cavity is presented.

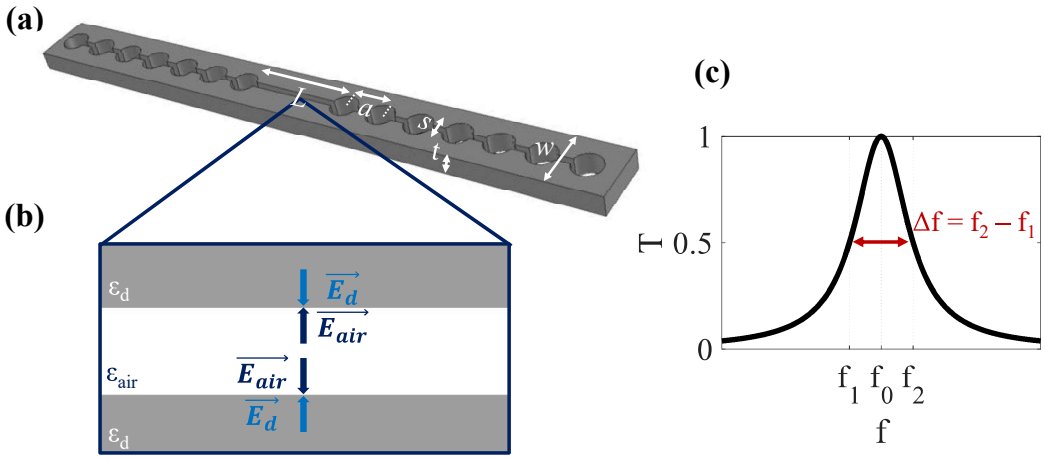

Figure 3.1 1D PhC nanobeam cavity. **(a)** Schematics of the structure. *L* is the cavity length, *w* is the beam width, *t* is the thickness and *a* is the lattice periodicity. **(b)** Field enhancement inside the cavity. **(c)** Representative Lorentzian resonance.

From the perspective of optical bio-sensing, our main aim is to sense the presence of the target analyte in terms of the variations in the refractive index of the background medium. The information of the background index change can be transferred to the optical domain via the 1D PhC nanobeam cavity by means of resonance frequency shift. In order to enhance the efficiency of the transduction, we need to maximize the area where the light interacts with the background medium. For that reason, we introduced a slot into the cavity, as represented in Figure 3.1(b), creating a 1D slot mode PhC nanobeam cavity. Introduced slot creates a field discontinuity for the light polarized normal to the boundary [31], [41]. When this is the case, the electric field is strongly localized in the slotted region, boosting the interaction between the light and the background medium. The field enhancement in the slotted regions is given in Equation 3.1 [75].

$$\boldsymbol{E_{air}} = \frac{\varepsilon_d}{\varepsilon_{air}} \boldsymbol{E_d} \tag{3.1}$$

By observing Equation 3.1, one can see that the electric field inside the slot is enhanced by a factor of ($\varepsilon_d/\varepsilon_{air}$). For a Si-air interface, therefore, the enhancement is around 12. The transmission of the cavity has a Lorentzian characteristic, as in Figure 3.1(c).

3.2 Figures of Merit

In order to characterize the cavity for bio-sensing purposes, there are several performance factors, namely, Q-factor, sensitivity, and mode volume [31], [76], [77].

3.2.1 Q-factor (Q)

Q-factor is one of the most important figures of merit for refractive index based optical bio-sensing. Simply, Q-factor is defined as the ratio of the energy stored inside the cavity to the energy lost during a single round trip inside the cavity [78]. Mathematically, for a resonant mode of the cavity, the Q-factor of the mode can be

expressed as the ratio of the resonant frequency to the full width half maximum (FWHM) of the mode as presented in Equation 3.2 [36].

$$Q = \frac{energy\ stored}{energy\ loss\ per\ cycle} = \frac{f_{res}}{\Delta f_{FWHM}} = \frac{\lambda_{res}}{\Delta\lambda_{FWHM}} \tag{3.2}$$

In Equation 3.2, f_{res} and Δf_{FWHM} are the resonant frequency and the FWHM in the spectral domain, while λ_{res} and λ_{FWHM} are the resonant wavelength and the FWHM in the wavelength domain. As it can be deduced from the equation, the Q-factor characterizes the sharpness of the resonant mode in the spectral domain. For the purpose of optical bio-sensing, a high Q-factor is desired. As the Q-factor gets higher, even tiny shifts in the resonance frequency can cause large variations in the power monitored at the output.

3.2.2 Sensitivity (*S*)

Sensitivity is also an important performance factor for optical bio-sensing applications. It characterizes the effect of a target analyte's presence in the background medium on the cavity resonance. It is defined as the ratio of the change of the resonant wavelength to the change in the background refractive index [27]. The performance factor can be expressed as in Equation 3.3 [79].

$$S = \frac{\Delta\lambda_{res}}{\Delta n_b} \tag{3.3}$$

In Equation 3.3, S is the sensitivity, and n_b is the background refractive index. Large sensitivity means that small changes in the background refractive index results in a large shift in the resonance wavelength.

3.2.3 Mode Volume (V_m)

The third performance factor is called the mode volume, and it is attributed to the confinement of the resonant mode in the spatial domain. The mode volume is used

for the characterization of the field localization inside the cavity [80]. Lower mode volume means intense light localization inside the cavity, enhancing the light-matter interactions, highly desirable for the optical detection of small molecules and nanoparticles. The mode volume of a resonance mode is given in Equation 3.4 [81].

$$V_m = \frac{\int \varepsilon |\boldsymbol{E}(\boldsymbol{r})|^2 \, dV}{\max[\varepsilon |\boldsymbol{E}(\boldsymbol{r})|^2]} \tag{3.4}$$

3.3 Cavity Design Procedure

During the design process of the 1D slot mode PhC nanobeam cavity, we aim to maximize the performance factors so that we can have an eminent device, which can be used as a refractive index based optical bio-sensor. For this purpose, we have mainly considered obtaining a high Q-factor. During the design, a deterministic recipe presented in [54] is followed.

There are two main components of the Q-factor of a cavity. The first one is the Q-factor determining the coupling loss to the waveguide, and the second one is the Q-factor by virtue of the coupling to the radiation modes. The total Q-factor of the cavity can be expressed in terms of these components, as in Equation 3.5 [54].

$$\frac{1}{Q_{tot}} = \frac{1}{Q_{wvg}} + \frac{1}{Q_{rad}} \tag{3.5}$$

In Equation 3.5, Q_{tot} is the total Q-factor of the cavity, while Q_{wvg} and Q_{rad} are the Q-factors associated with the coupling and radiation losses, respectively. Therefore, to increase the total Q-factor of the cavity, we need to increase its components. In order to increase the Q_{wvg}, all we need is to increase the number of mirrors segments in the cavity. When this is the case, the 1D PhC will approach its ideal infinite form and will reflect the light better. Therefore, the portion of the light coupled to the waveguide will be decreased, leading to an increased Q_{wvg}.

In order to increase the Q_{rad}, we need to minimize the coupling to the radiation modes of the cavity. To realize that, there are three main aspects to which we need to pay attention.

- Constant lattice periodicity
- Gaussian-like attenuation profile
- Zero cavity length

Constant lattice periodicity: The first rule that we need to follow is not to change the lattice periodicity through the structure. If the periodicity is altered through the structure, the mode mismatch occurs between the mirror segments, and the scattering of light at the segment boundaries results in increased coupling to the radiation modes of the structure; hence, decreased Q-factor. For that reason, the lattice periodicity must be kept constant through the device.

Gaussian-like attenuation profile: In order to minimize the number of spatial Fourier harmonics of the cavity mode inside the light cone, a Gaussian-like attenuation profile must be created along the cavity. In a classic 1D PhC nanobeam cavity, in resonance, the mode attenuates from the cavity center to the mirror ends with an exponential attenuation profile of $e^{-\kappa x}$, where κ is called as the mirror strength, i.e., the imaginary part of the complex wave vector inside the bandgap. Therefore, in order to create a Gaussian-like attenuation, we need to obtain a linearly increasing mirror strength, in the form of $\kappa = \alpha x$. When this is the case, we have an attenuation profile of $e^{-\alpha x^2}$. The mathematical expression of the mirror strength can be derived via plane wave expansion. The final expression is given in Equation 3.6 [82].

$$\gamma = \sqrt{\frac{(\omega_a - \omega_d)^2}{(\omega_a + \omega_d)^2} - \frac{(\omega_{res} - \omega_m)^2}{{\omega_m}^2}} \tag{3.6}$$

In Equation 3.6, γ is the mirror strength. ω_a, ω_d, ω_m, and ω_{res} are the air band edge frequency, dielectric band edge frequency, mid-gap frequency, and the resonant frequency, respectively. It can be seen in Equation 3.6 that the mirror strength is strongly dependent on the band diagram characteristics of the individual mirror

segments; therefore, the geometry parameters. Indeed, the linear increase in the mirror strength can be realized by quadratically tapering the hole radius from the center to the mirror ends. The formula of the hole radii tapering is given in Equation 3.7 [81].

$$r_i = r_1 + \frac{(i-1)^2}{(n-1)^2}(r_1 - r_n) \tag{3.7}$$

In Equation 3.7, i is an integer which can take values from 1 to n, where n is the number of mirror segments at one side of the cavity, and r_i is the hole radius of the i^{th} mirror segment from the center.

Zero cavity length: The cavity length is the distance between the Bragg reflectors. The field profile of the resonant mode strongly depends on the cavity length. Therefore, the components of the wave vector of the cavity resonance can be controlled via the cavity length. The previous research indicates that the number of spatial Fourier harmonics within the light cone of the structure is minimized when the cavity length is set as zero, i.e., the distance between the center mirror segments is the same as that of others. Moreover, zero cavity length further reduces the mode volume of the cavity resonance.

In the light of these rules, a high Q-factor 1D PhC nanobeam cavity can be designed by following the steps given below.

- The first step is to choose the target resonance frequency (f_{res}). The target frequency must be chosen %10 larger than the desired frequency in order to compensate for the detuning due to the finite number of mirror segments.
- The second step is to determine the thickness (t) of the nanobeam as it is the most restricted parameter due to fabrication-related considerations.
- The third step of the design process is to determine the lattice periodicity (a). The lattice periodicity can be determined by setting it to a value around half of the resonant wavelength inside the structure.

- Fourth, the width of the nanobeam must be set. The value of the width is chosen by taking the number of modes into consideration. The higher value of the width pulls the bands down, resulting in the inclusion of the higher order modes. Conversely, a lower beam width results in a decreased light confinement, leading to the degraded Q-factor.
- In this design, the resonance frequency of the cavity approaches to the dielectric band edge frequency of the center mirror segment. For this purpose, the radius of the center hole must be set in accordance with the target resonant frequency.
- Next, the radius of the last mirror segment in the structure must be determined. The value of the hole radius can be chosen as the radius with the maximum mirror strength.
- Afterwards, the number of mirror segments must be determined in order to obtain a sufficient Q_{wvg} value.
- Finally, the radii of the intermediate mirror segments must be determined by applying the formula given in Equation 3.7.

3.4 Results and Numerical Analyses

3.4.1 Band Diagram Simulations

In order to initiate the design process of the 1D slot mode PhC nanobeam cavity, we set the target frequency as 193.5 THz (1550 nm) in order to operate in the telecom wavelength range. Considering the detuning due to the finite number of holes, we added an offset to the target frequency by %1, corresponding to a value of 195.4 THz (1535 nm). Also, the thickness of the nanobeam is preset as 220 nm based on the available wafers in the fabrication facility.

The remaining design parameters are determined by conducting photonic band diagram simulations via MIT Photonic Bands (MPB) software package [51]. Through the simulations, the nanobeam material is chosen as Silicon (n_{Si} = 3.48), as

the devices are planned to be fabricated on a Silicon-on-Insulator (SOI) wafers. The background medium is determined as deionized water, whose refractive index (n_W) is chosen as 1.318 around the telecom wavelength range.

In order to determine the lattice constant (a), we need to estimate the effective refractive index (n_{eff}) of the resonant mode. We know that it will take a value between n_{Si} and n_W. Moreover, it will be close to n_W, as the light is expected to be localized mostly in the low index regions. Therefore, as a starting point, n_{eff} is roughly set as 2, corresponding to a lattice constant of ~380 nm.

Next, the value of the nanobeam width is determined. An initial value of 600 nm is set based on the previous research in the literature.

The radius of the center hole and the slot width are determined in order to set the dielectric band edge frequency to the target resonance frequency. For this purpose, 3D unit cell simulations are conducted via MPB [51]. The 2D cross-sections of the simulated unit cell are given in Figure 3.2(a)-(b).

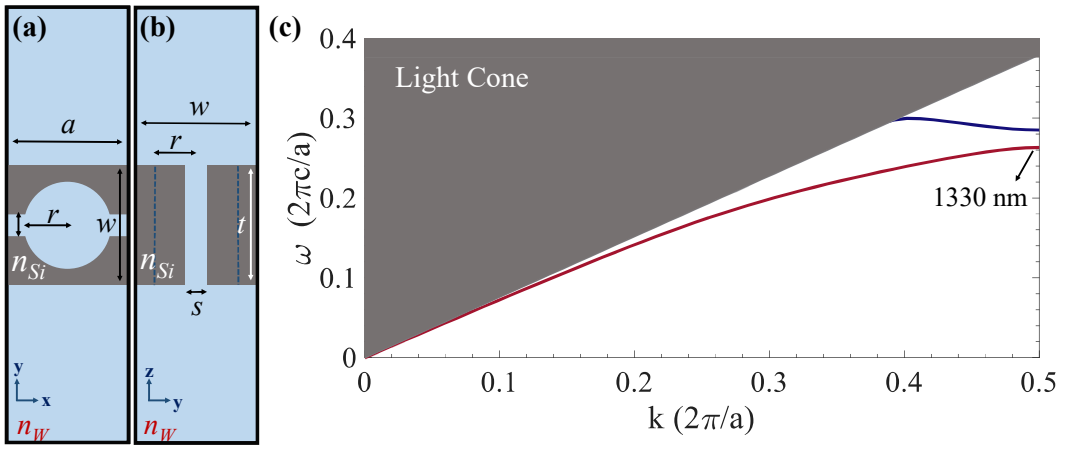

Figure 3.2 Unit cell design process. **(a)** The x-y cross-section of the unit cell. **(b)** y-z cross-section of the unit cell. **(c)** The band diagram of the unit cell with the initial parameters.

In addition to the parameters set above, we have initiated our band diagram analysis by determining the hole radius and the slot width as 120 nm and 50 nm, respectively.

The corresponding photonic band diagram is presented in Figure 3.2(c). As it can be seen in Figure 3.2(c), the bandgap needs to be increased, and the bands must be pulled down. For this purpose, the hole radius can be increased; however, the value of the lattice constant may prevent the sufficient increase of the hole radius. For that purpose, the lattice constant is swept from 380 nm to 500 nm, and the behavior of the band edge frequencies are depicted in Figure 3.3.

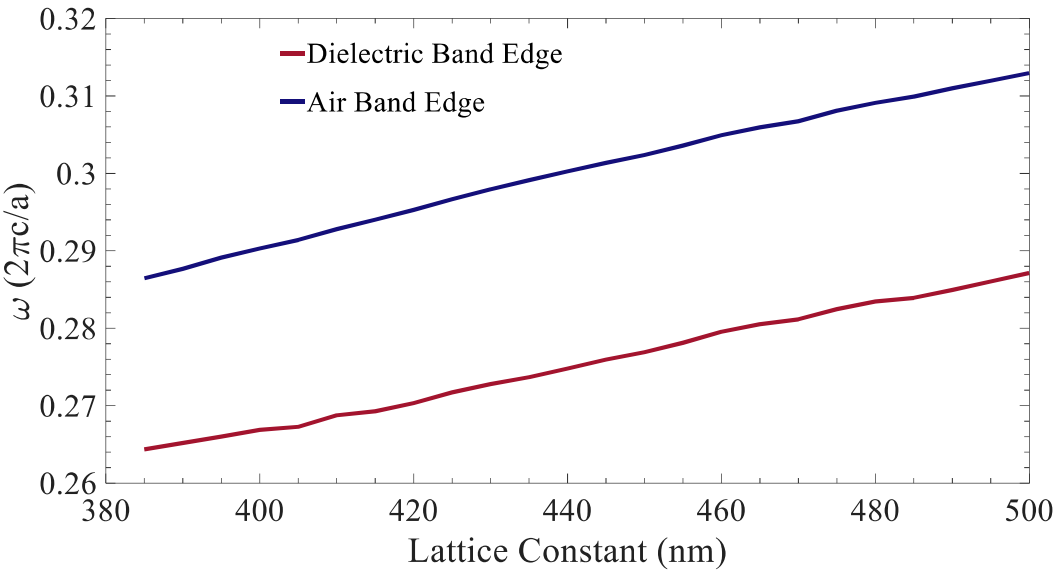

Figure 3.3 The characteristics of band edge frequencies with respect to the lattice constant.

By observing the trend in Figure 3.3, the lattice constant is chosen as 480 nm. For this value of *a,* there is enough room for the sweep of the hole radius and the target frequency is close to the telecommunication range. Note that, in this configuration, the dielectric band edge frequency is lower than the targeted value, as the increase in the radius will result in a blue-shift of the bands.

Afterwards, we optimized the nanobeam width by sweeping the value of *w*, with the updated value of *a*. The characteristics are presented in Figure 3.4. The nanobeam is widened in order to pull the modes down so that a sufficient margin can be inserted

between the resonant mode and the light line. Correspondingly, the width of the nanobeam is updated as 670 nm.

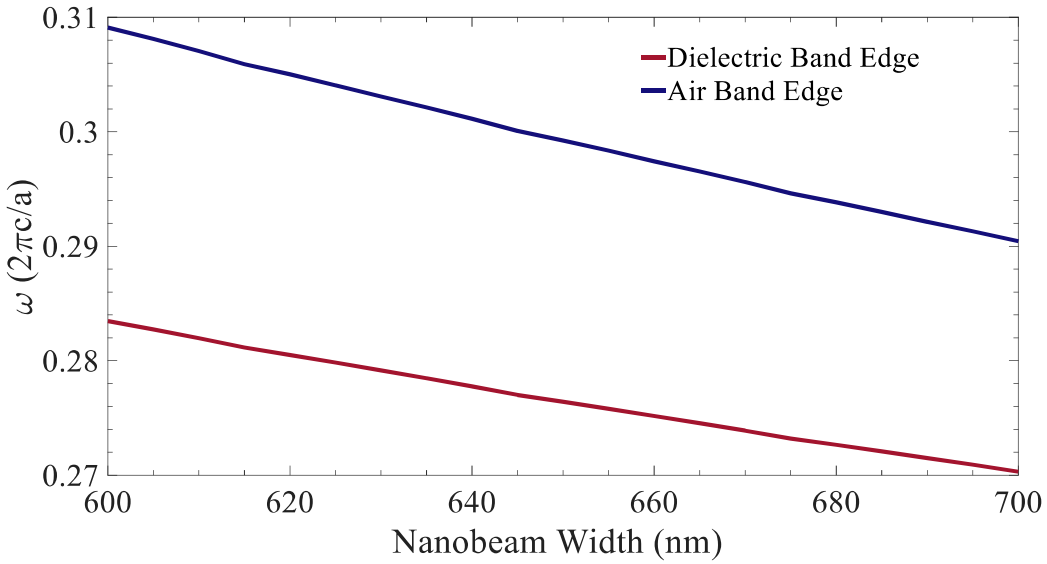

Figure 3.4 The variation of band edge frequencies with respect to the nanobeam width.

Afterwards, the hole radius is swept in order to set the dielectric band edge frequency to the targeted value. The corresponding characteristic is given in Figure 3.5.

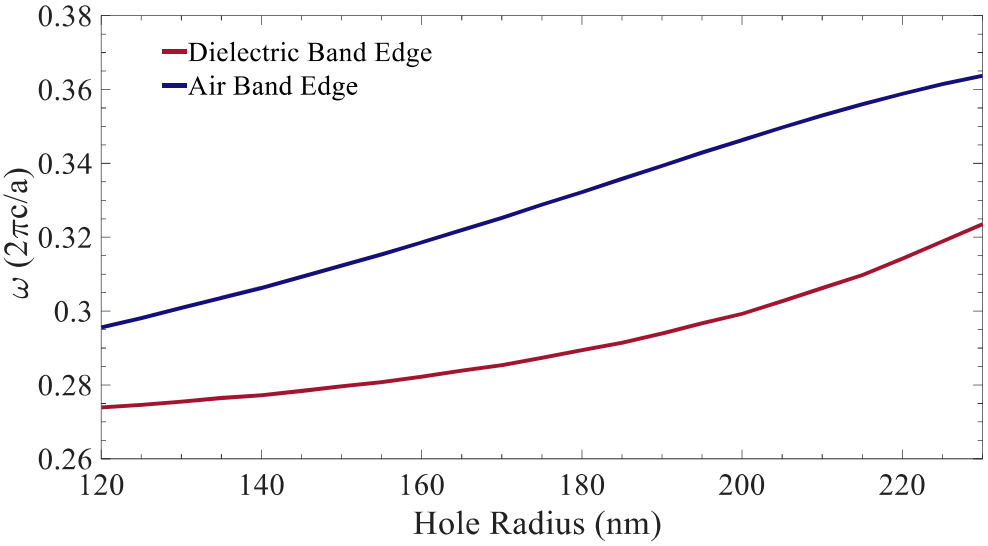

Figure 3.5 The behavior of band edge frequencies with respect to the hole radius.

As it can be seen in Figure 3.5, the bandgap widens as the hole radius is increased. Moreover, the bands are blue-shifted. Based on the sweep data, the radius of the center mirror segment hole is determined as ~220 nm, which corresponding to a target resonance wavelength of ~1532 nm.

Apart from the hole radius, we also swept the slot width parameter in order to observe its effect on the band diagram. The change in the band edge frequencies with changing slot width is presented in Figure 3.6. Based on our observations, we decided to keep the initial value (50 nm), as increasing it drastically closes the bandgap, while further decreasing it would result in impractical implementation in terms of fabrication.

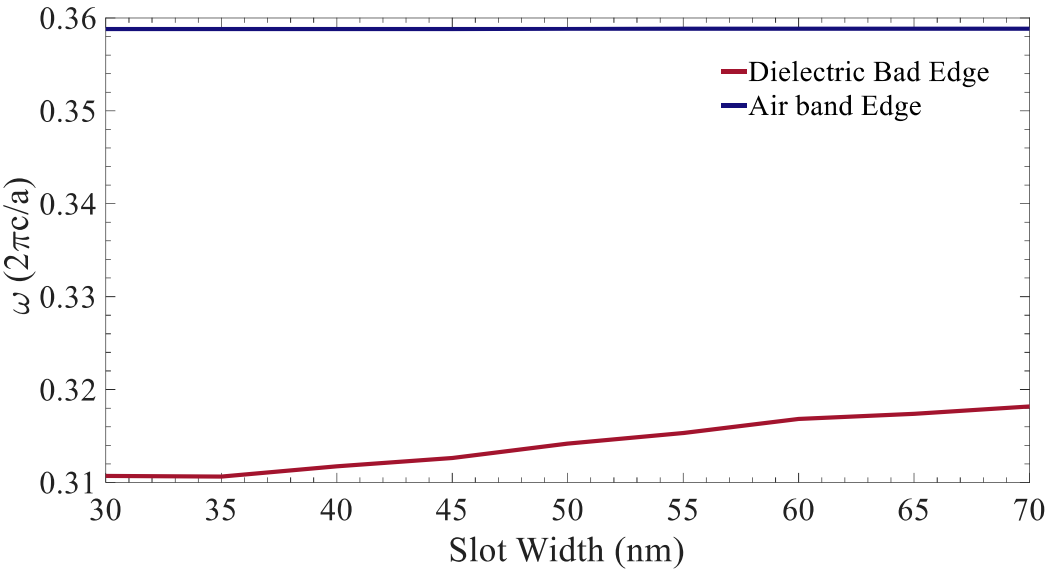

Figure 3.6 The effect of the slot width on the band edge frequencies.

After setting the entire parameters for the center unit cell, our next goal is to set the radius of the segments at the end of the mirrors. For this purpose, we calculated the mirror strength for different radii by applying the formula given in Equation 3.6. In Figure 3.7, the mirror strength characteristics are given. We determined the value of the last hole radius around 190 nm, aiming to maximize the mirror strength.

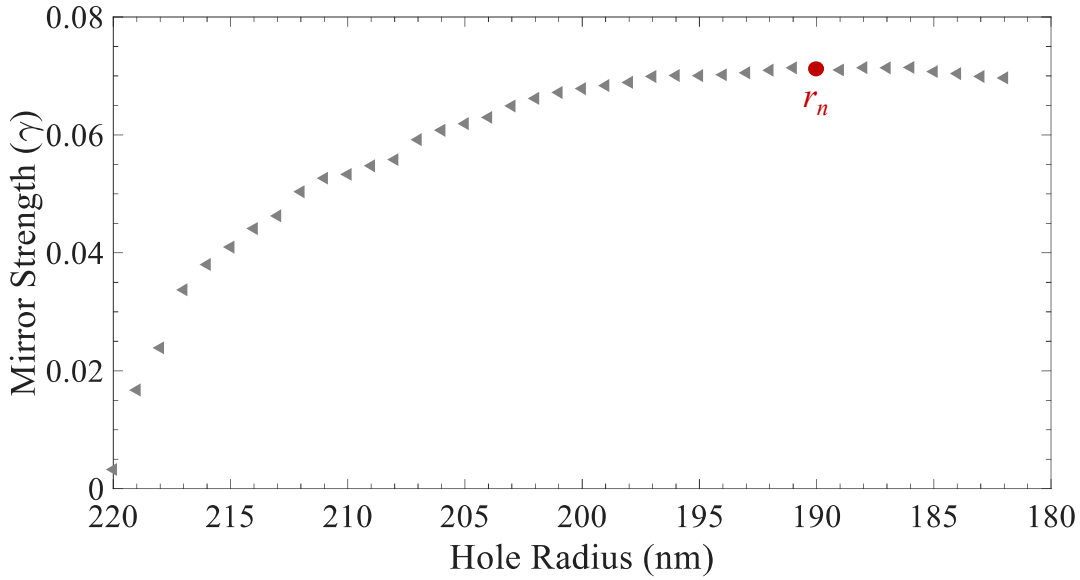

Figure 3.7 Mirror strength with respect to the hole radius.

After setting the radius of the last mirror segment, the radii of the remaining holes can be determined via the tapering formula given in 3.7. With this step, the necessary parameters for the cavity design are determined. The list of parameters can be observed in Table 3.1. The band diagrams of the center mirror segment and the last mirror segment are presented in Figure 3.8.

Table 3.1 Specified Design Parameters of the Cavity

Design Parameter	Value (nm)
Lattice Constant	480
Nanobeam Width	670
Nanobeam Thickness	220
Slot Width	50
Center Hole Radius	220
Last Hole Radius	190

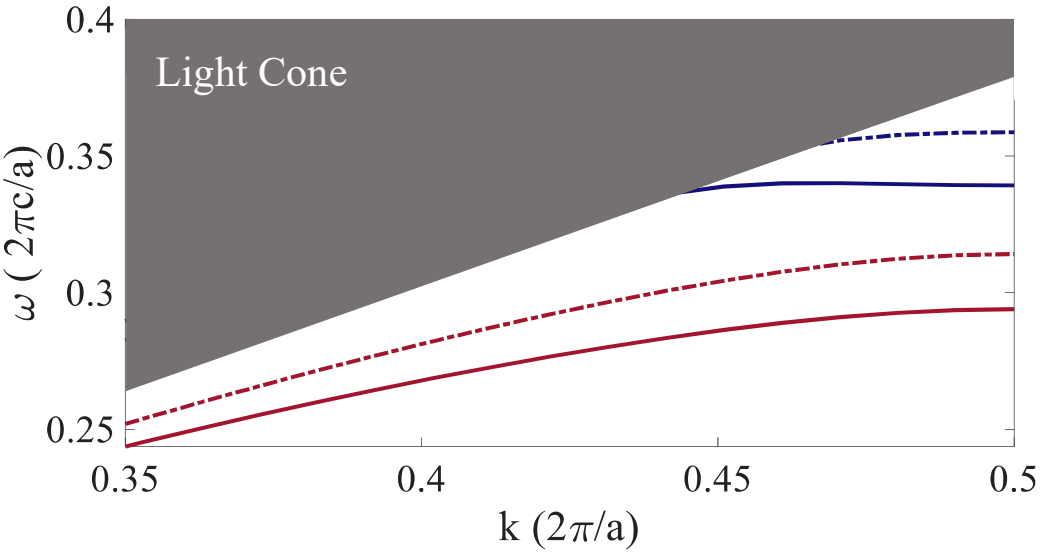

Figure 3.8 The band diagram of the center and end mirror segments. The dark red lines indicate the dielectric bands, while the dark blue lines depict the air bands. The dashed and the continuous lines represent the bands of the center and end mirror segments, respectively.

3.4.2 Mode Analysis and FDTD Simulations

After determining the design parameters, finite difference time domain (FDTD) simulations have been conducted in order to observe the fundamental resonance via MIT Electromagnetic Equation Propagation (MEEP) software package [83]. Thirty mirror segments at both sides are quadratically tapered; moreover, ten additional mirrors are appended at the mirror ends in order to further increase the Q-factor. The schematic of the simulated structure is given in Figure 3.9(a). With this configuration, the cavity exhibits a fundamental resonance at a wavelength of 1535 nm with a Q-factor of ~2×10^5. The mode profile of the fundamental resonance for the TE-like excitation is presented in Figure 3.9(b)-(c) from different cross-section views. A line slice is taken through the propagation direction, and a sinusoidally-modulated Gaussian fit is applied. The slice data and the fit are presented in Figure

3.10. As it can be seen, the cavity exhibits a Gaussian-like attenuation, which is the key factor for the high Q-factor.

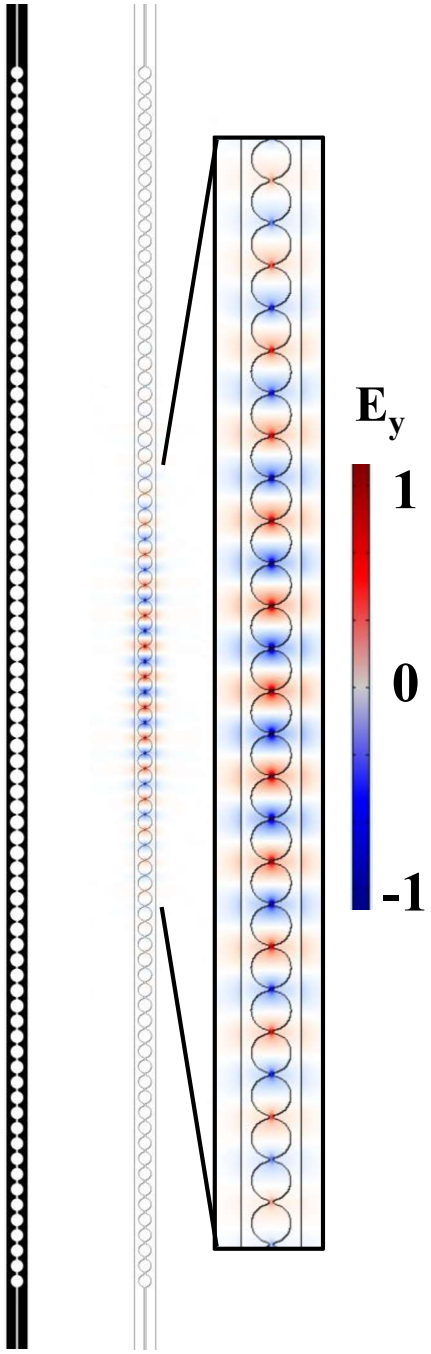

Figure 3.9 FDTD analysis of the designed cavity. **(a)** The refractive index distribution of the simulation environment. **(b)** The E_y mode profile of the fundamental resonance of the cavity. Inset: Zoom-in to the cavity center.

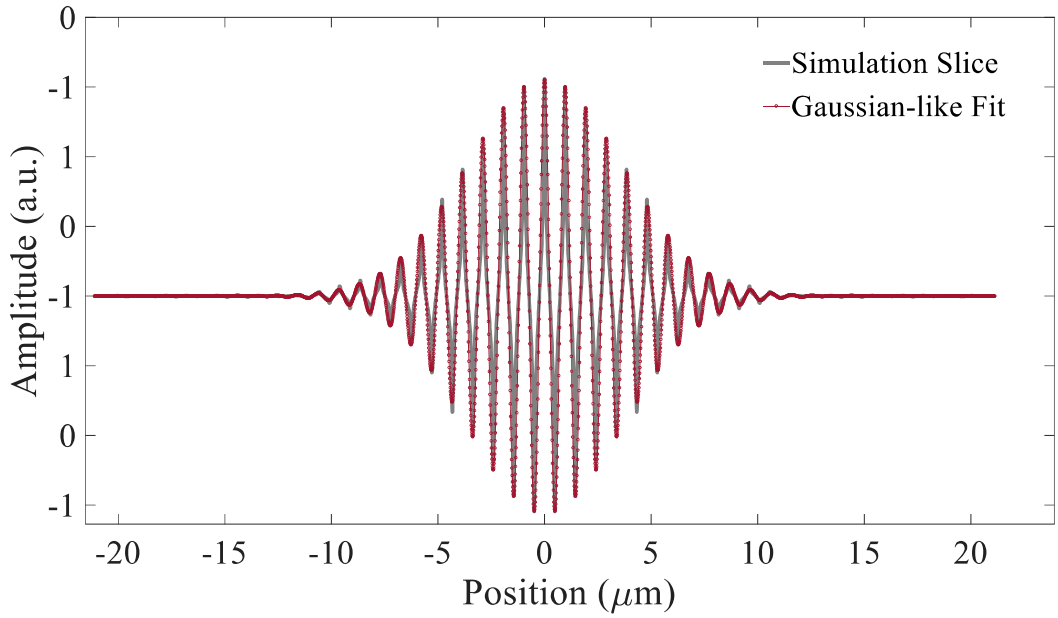

Figure 3.10 The slice of the cavity mode profile through the propagation direction and Gaussian-like fitting. The grey thick line depicts the field data, while the dotted red line indicates the Gaussian-like fitting.

Having obtained the resonant profile, our next move is to characterize the device performance as an optical bio-sensor. However, before doing that, we simplified our cavity, as obtaining high-resolution data with the present configuration notably increases the computation cost. For this reason, we reduced the number of mirror segments to fifteen on both sides. The simplified cavity is presented in Figure 3.11(a). The new configuration has a fundamental resonance around 1544 nm, as reducing the number of mirror segments causes a slight deviation of the resonance frequency from the dielectric band edge frequency of the center mirror segment. The mode profile of the cavity resonance can be observed in Figure 3.11(b)-(c).

We characterized the cavity performance as a bio-sensor and analyzed it in terms of the previously mentioned performance factors. The intrinsic Q-factor of the cavity is calculated as ~8200, with fifteen mirror pairs at the sides of the cavity. Afterwards, the sensitivity of the cavity is examined by sweeping the background index of the

medium from 1.318 to 1.34. The corresponding relationship is depicted in Figure 3.12. From the slope of the line in Figure 3.12, the sensitivity is calculated as 667 nm/RIU. Finally, the mode volume of the cavity resonance is calculated by the formula given in Equation 3.4. The fundamental resonance of the cavity has a mode volume of 0.4891 in units of the cubic resonant wavelength in Si. Calculated value supports the sub-wavelength light confinement inside the cavity. The performance data of the cavity are tabulated in Table 3.2.

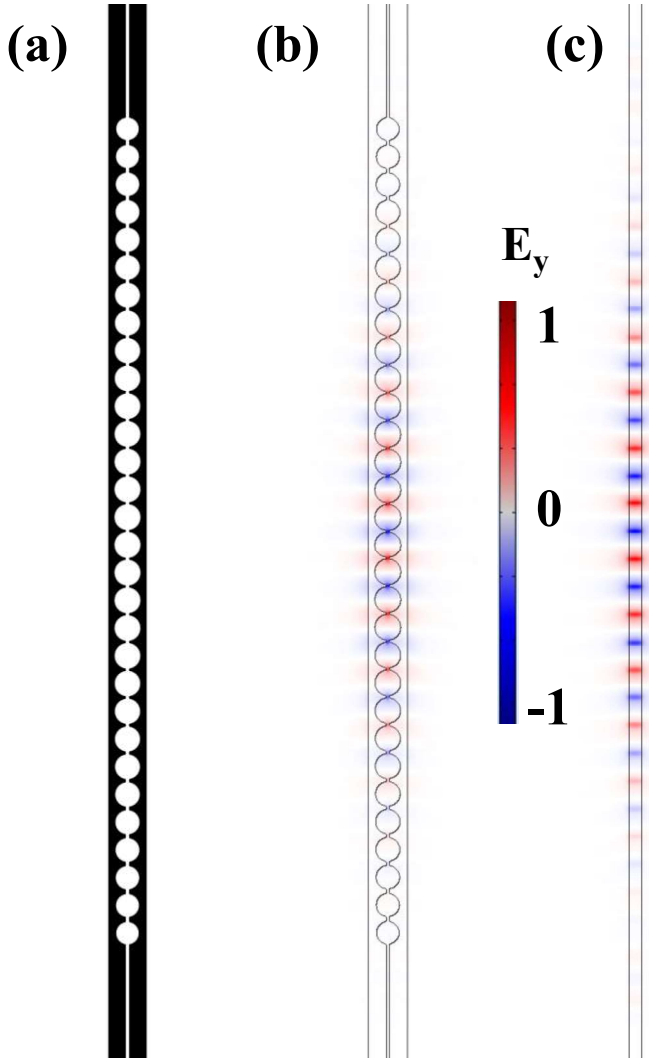

Figure 3.11 FDTD analysis of simplified cavity. **(a)** The schematic of the simplified configuration. **(b)** Mode profile in the x-y plane. **(c)** Mode profile in the x-z plane.

Table 3.2 Cavity Performance as a Bio-sensor

Performance Factor	Value
Q-factor	8200
Sensitivity	667 nm / RIU
Mode Volume	0.4891 $(\lambda_{res}/n_{Si})^3$

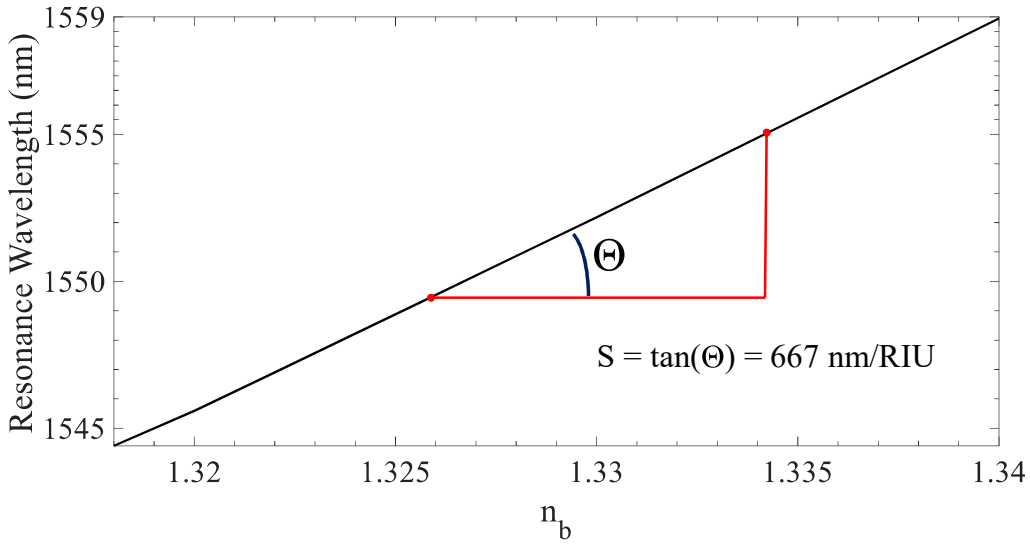

Figure 3.12 The variation of resonance wavelength with respect to the background refractive index.

Finally, the transmission spectrum of the structure is extracted by utilizing FDTD simulations. The spectrum is provided in Figure 3.13. In Figure 3.13, the fundamental resonant mode used for optical bio-sensing is seen.

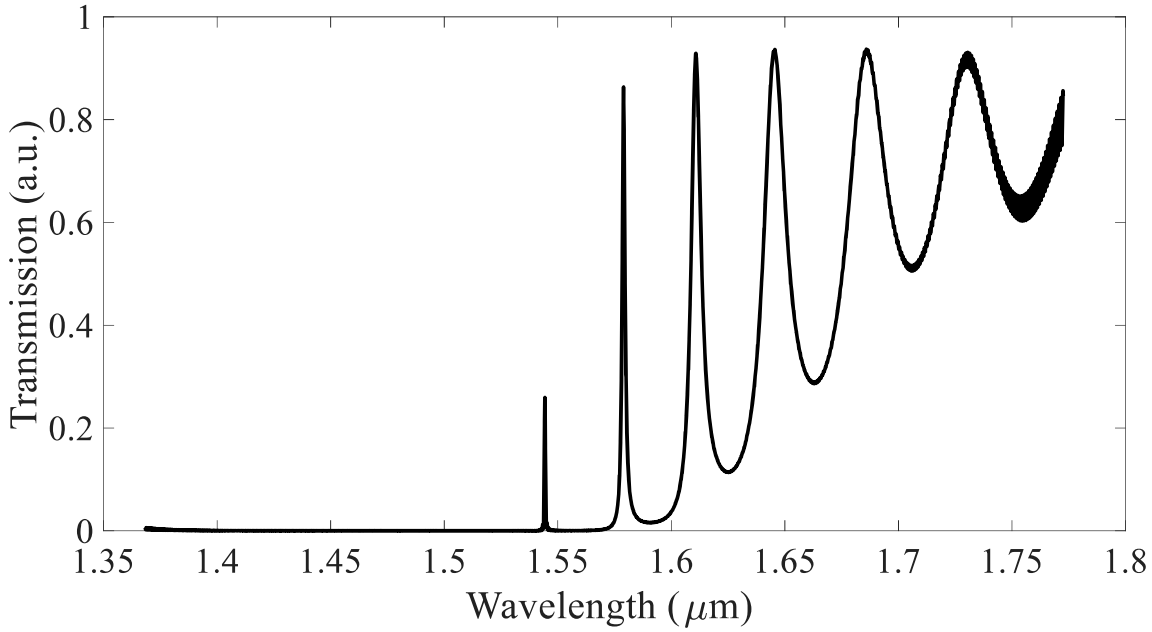

Figure 3.13 Transmission spectrum of the simplified cavity.

CHAPTER 4

SENSITIVITY ENHANCEMENT VIA OPTOMECHANICALLY INDUCED OPTICAL FEEDBACK

This chapter covers the detailed explanation and the analysis of a method utilized in order to enhance the performance of the slot mode 1D PhC nanobeam cavity bio-sensor. The motivation of the approach is demonstrated. The operation principle of the applied enhancement method is delivered. The amount of enhancement is quantified via FDTD and Finite Element Method (FEM) simulations.

4.1 Q-factor vs Sensitivity Trade-Off

In Chapter 3, the design methodology of a slot mode 1D PhC nanobeam cavity is presented in detail. Obviously, these structures are highly advantageous for refractive index based optical bio-sensing applications, as they possess high values in terms of the performance factors mentioned before [54], [76], [84]. For an eminent optical bio-sensing operation, all of the performance factors must be high at the same time. The design parameters must be chosen carefully in order to obtain high values of performance factors, as in the previous chapter. Especially, the slot width is a critical parameter, as it affects all of these factors. In our case, we tried to choose the smallest practical value for the slot width as it maximizes the Q-factor. However, decreasing the slot width degrades one of the performance factors, sensitivity, as the area where the light and the background medium interact is shrunk. Likewise, enlarging the slot causes degradation on the Q-factor, while boosting the sensitivity. Therefore, an intrinsic trade-off exists between these two performance factors [81]. Such a trade-off can be observed in Figure 4.1 for the device designed in the previous chapter.

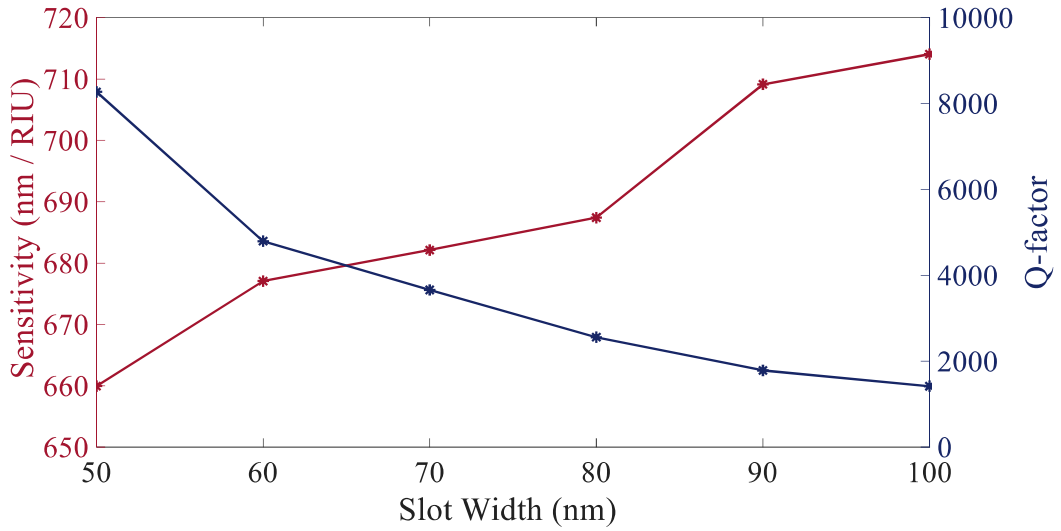

Figure 4.1 The trade-off between the sensitivity and Q-factor of the cavity with respect to the slot width.

There have been numerous approaches to the design of these kinds of structures. Most of them include the exhaustive parameter search approach, where brute-force trials are conducted until an optimal value is obtained in terms of both performance factors [38], [41], [54], [81]. Therefore, the necessity of an alternative approach definitely exists, which gives us the motivation to conduct the study presented in this chapter. As an alternative to the present static parameter search methods, we proposed an approach that dynamically tunes the slot width by utilizing the transverse optical forces generated inside the cavity. By slightly modifying the device geometry, we implanted an optical positive feedback mechanism into the cavity, triggered by the presence of the target analyte at the background. When triggered, the feedback mechanism enhances the effects of the target analyte on the cavity characteristics, resulting in improved device performance in terms of the previously defined figures of merit.

4.2 Operation Principle and the Optomechanical Feedback

In order to enhance the performance of the bio-sensor, a positive feedback loop is appended to the cavity, as presented in Figure 4.2(a)-(b). For the operation of optical bio-sensing, there are two inputs of the system, namely the probe signal and the pump signal. The probe signal is utilized for monitoring purposes, and its frequency is matched to the frequency where the rate of spectral change is maximum around resonance. In this way, any spectral change induced by the target analyte invasion can be detected by means of power read at the photodetector output. Therefore, the probe signal propagates through the cavity, and it is collected at the output port. On the other hand, the pump is the signal utilized to generate the transverse optical gradient forces inside the cavity. Its frequency can take any value, residing outside the bandgap of the cavity. The pump signal propagates through the cavity, and it is coupled to the feedback loop, depicted in Figure 4.2(a)-(b), via a directional coupler. The light coupled to the loop propagates back to the input and interferes with the light coming from the input.

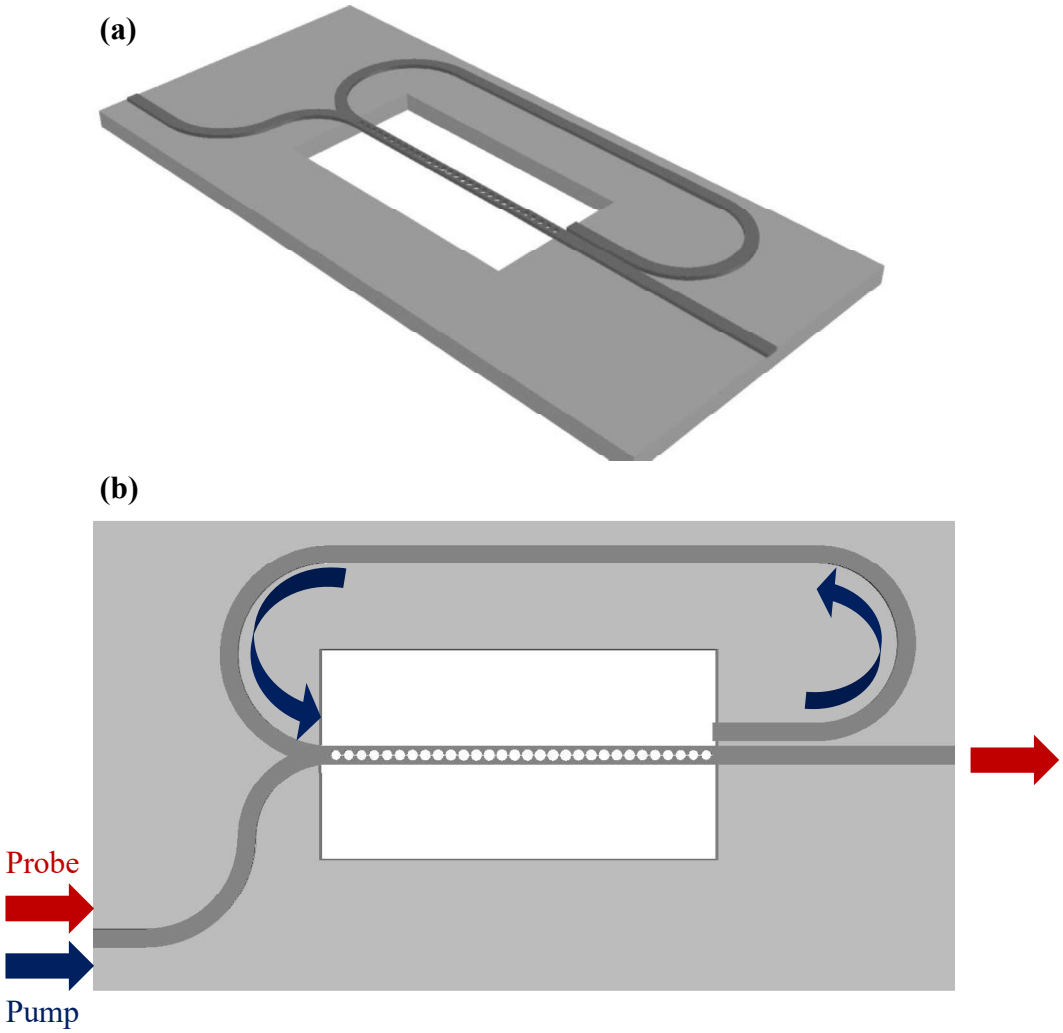

Figure 4.2 **(a)** Isometric view of the device with the feedback loop. **(b)** Top view of the optomechanically enhanced bio-sensor.

The performance enhancement mechanism is controlled by tuning the interference of the pump light at the input. Initially, the phase accumulated through the feedback loop is arranged so that the pump light interferes destructively, defined as the idle state. In the idle state, the power of the pump light injected to the cavity is zero; hence, the optical force generated inside the cavity is also zero. When the target analyte enters the medium, the effective refractive index of the background medium is increased, meaning that the phase accumulated through the feedback loop is also modified, as the background medium constitutes the top cladding of the feedback

loop waveguide. The altered phase leads to the disturbance of the destructive interference at the output, and a finite force is created in the cavity. The generated force pulls the sides of the nanobeam towards each other and reduces the width of the nanobeam. When the slot width is narrowed, the effective refractive index is further increased, resulting in a further increase in the transverse optical gradient force inside the cavity. Increased force further decreases the slot width, causing the slot width to be further shrunk. Hence, there exists positive feedback between the optical force and the slot width shrinkage. These two events follow each other repeatedly until a stable condition is realized. The structure reaches its steady-state when the pump light fed back to the input interferes constructively, namely the equilibrium state. The block diagram representation of the feedback loop is given in Figure 4.3.

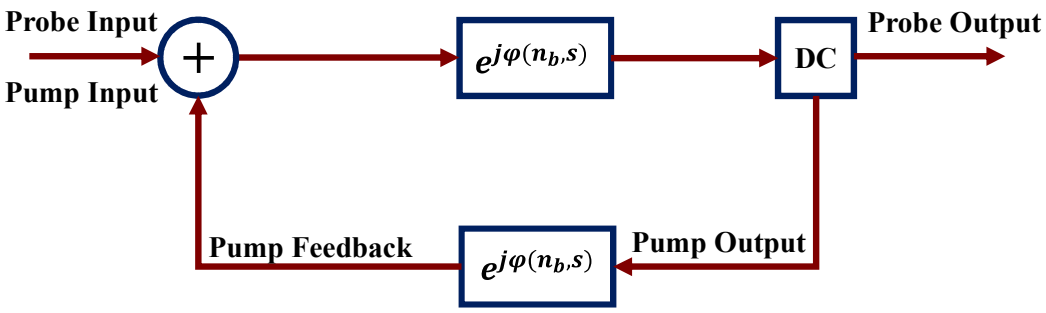

Figure 4.3 The block diagram representation of the device operation and the performance enhancement feedback loop.

With the help of the feedback loop presented in Figure 4.3, the sensitivity and the Q-factor of the cavity are enhanced simultaneously, i.e., the trade-off is broken. The enhancement of the sensitivity is attributed to the additional resonant wavelength shift induced by the shrinkage of the slot width. The optomechanical feedback reduces the width of the slot during the device operation. The slot width reduction causes a red-shift on the resonance wavelength, shifting the resonant wavelength in the same direction as the target analyte intrusion. Therefore, the total change in the resonance wavelength for a given change in the background refractive index is increased, corresponding to enhanced sensitivity. The reduction of the slot width also

enhances the Q-factor, as smaller slot width yields stronger light confinement in the cavity.

4.3 Numerical Analyses and Results

In this part, the analysis of the amount of the performance enhancement is presented, in addition to the optical force calculations. Also, the effect of the initial slot width on the enhancement level is discussed.

4.3.1 Optical Force Calculations

Before analyzing the level of performance enhancement of the bio-sensor, the optical force generated inside the cavity is calculated in order to determine the amount of power required to reduce the slot width sufficiently. As already explained in detail in Chapter 2, the optical force can be calculated by the formula given in Equation 2.28. For that purpose, we have analyzed the variation of the effective refractive index with respect to the slot width. The FEM simulations are conducted and the results are shared in Figure 4.4(a). The effective refractive index decreases with the increasing slot width. We also analyzed the effect of the background index on the trend of the variation and presented it in Figure 4.4(a). The effective refractive index variation has an offset for the higher background index; however, the trend is similar. As the next step, we calculated the normalized optical force by utilizing Equation 2.28. The data can be observed in Figure 4.4(b). By looking at the data, one can deduce that the generated force does not significantly change with the initial value of the background refractive index.

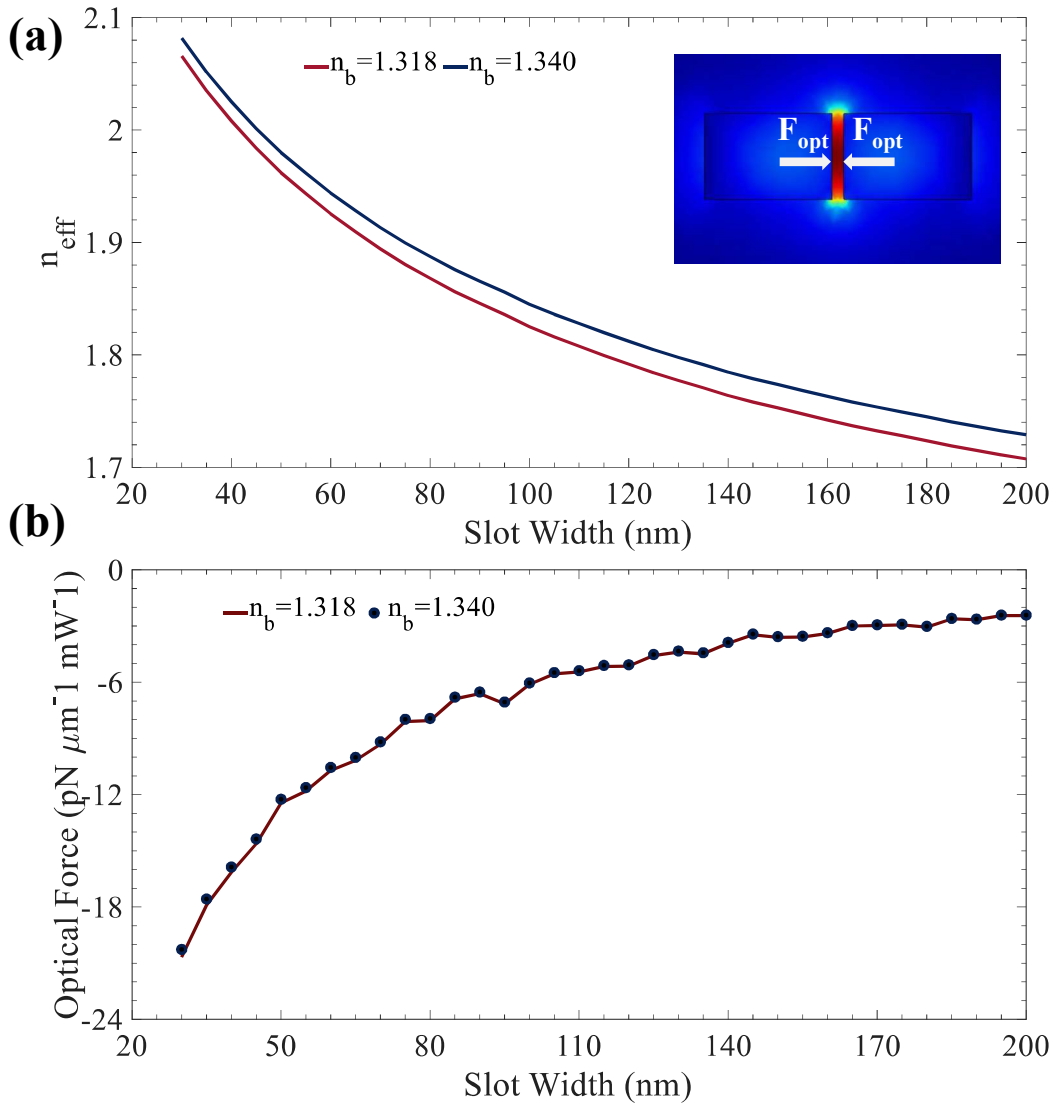

Figure 4.4 Optomechanical analysis. **(a)** The variation of the effective refractive index with respect to the slot width for different background refractive indices. **(b)** The normalized transverse optical gradient force with respect to the slot width for different background refractive indices.

4.3.2 Pump Signal Interference

The interference of the pump light through the feedback loop is calculated by the FDTD simulations in MEEP [83]. The device is excited with a continuous beam at a

wavelength of 1686 nm, and a 1D slice of the field profile is taken at the output of the cavity after the pump light interferes with itself at the input. The simulation is repeated for two different background refractive index values of 1.318 and 1.360, where the results are presented in Figure 4.5.

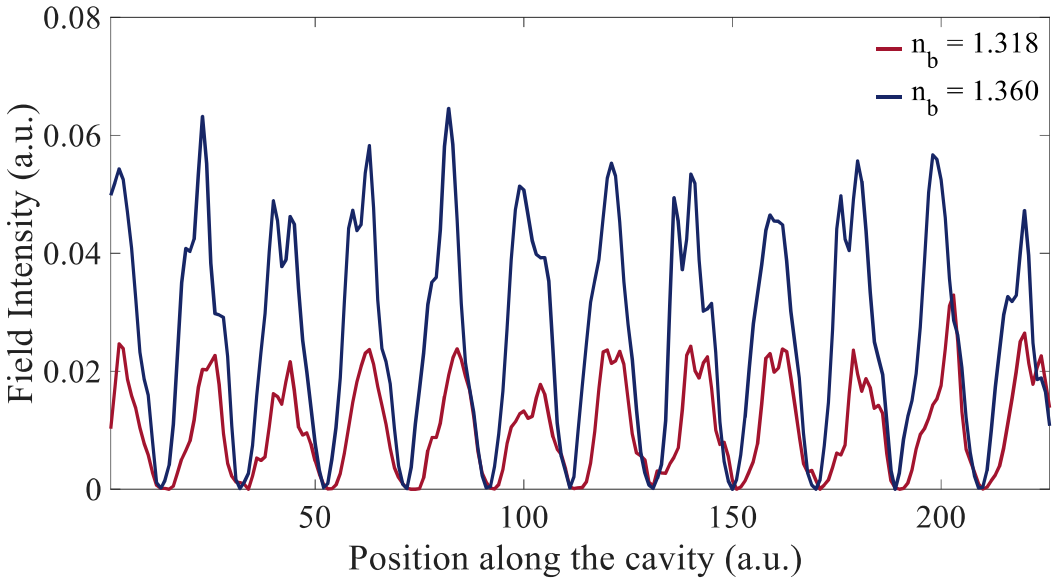

Figure 4.5 The demonstration of the pump interference at the device output. The combined intensity at the output is presented for different background refractive index values.

As one can see in Figure 4.5, the pump intensity significantly changes with the changing background refractive index, highly suitable for the triggering of the optical positive feedback between the shrinkage of the slot width and the increase of the effective refractive index of the system.

4.3.3 Optomechanical Deflection

The intrusion of the target analyte into the background medium triggers the mechanism leading to the generation of transverse optical forces inside the cavity, as calculated in normalized values in Section 4.3.1. The optical force causes the sides of the nanobeam to deflect towards each other, reducing the slot width. In order to

calculate the deflection, the absolute optical force value is required, necessitating the determination of the power of the pump input and the device length. Unlike the non-resonant optomechanical systems, in our structure, the pump power, hence the optical force depends on the position along the cavity, as the field is mostly localized in the slotted regions. For that reason, we have slightly modified the formula in Equation 2.28. The modified version is given in Equation 4.1

$$F(g) = \frac{\int_0^L P_{pump}(x)dx}{c}\frac{\partial n_{eff}}{\partial g} \cong \frac{P_{pump}L_{eff}}{c}\frac{\partial n_{eff}}{\partial g} \tag{4.1}$$

In Equation 4.1, P_{pump} is the power of the pump beam injected into the system, while L_{eff} is the effective length of the cavity, incorporating the cavity portions where the pump field is present. Note that the input power and the device length can be interchangeably arranged, as their multiplication determines the absolute value of the optical force. Moreover, the effective length of the structure can be flexibly played by appending slot waveguides at the cavity ends. Correspondingly, we have made an iterative optical force analysis via the algorithm implemented by our group [62]. For a 20 nm total deflection, the required pump power is around 10 mW, with additional 11.3 μm long slot waveguides appended at both sides. The deflection profile for such a case is given in Figure 4.6(a). Additionally, we also analyzed the case, where both sides of the nanobeam deflect towards each other by 5 nm. In this case, the required power drops to 6.1 mW. The profile of the smaller deflection case can be seen in Figure 4.6(b).

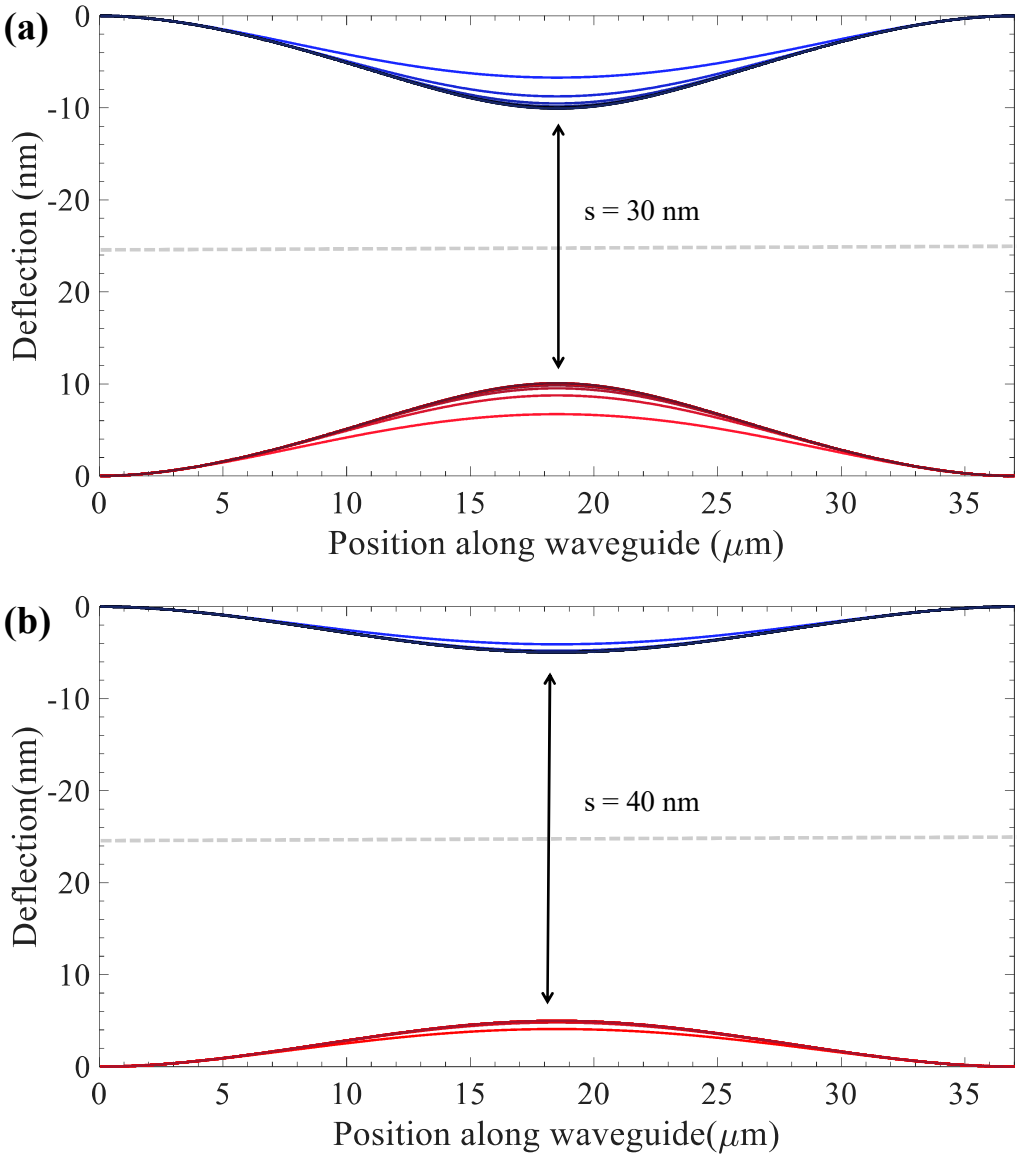

Figure 4.6 Iterative optomechanical deflection analysis of the cavity with 11.3 µm slot waveguides appended at both sides. Red and blue lines present the deflection profile of the sides of the nanobeam and the iteration lines get darker with the increasing iteration number. **(a)** 20 nm total deflection of the nanobeam sides. **(b)** 10 nm total deflection of the nanobeam sides.

4.3.4 Sensitivity Enhancement

The enhancement system is initiated when the target analyte enters the background medium. When this is the case, the resonant wavelength shift due to the increase of the background refractive index is combined with the shift coming from the reduction of the slot width. Therefore, the overall sensitivity of the optical bio-sensor is enhanced. We analyzed the total shift of the resonant wavelength with respect to the change in the background index for different amounts of beam deflection. The resonant wavelength data for different background indices and the slot width are provided in Table 4.1.

Table 4.1 Resonant wavelength characteristics for various n_b and s values

s (nm) / n_b *(RIU)*	*50*	*40*	*30*
1.318	1544.3 nm	1556.1 nm	1570.1 nm
1.320	1545.6 nm	1557.4 nm	1571.4 nm
1.322	1546.9 nm	1558.7 nm	1572.6 nm
1.324	1548.2 nm	1560.0 nm	1573.8 nm
1.326	1549.5 nm	1561.3 nm	1575.1 nm
1.328	1550.9 nm	1562.5 nm	1576.3 nm
1.330	1552.2 nm	1563.8 nm	1577.6 nm

Having analyzed the spectral behavior of the cavity for different values of the slot width, we extracted the level of enhancement for different beam deflections. The enhancement of the sensitivity is examined for 10 nm and 20 nm deflections. Note that the amount of the deflection is determined by properly setting the pump power and the suspended region length. The shifts in the resonant wavelength are given in Figure 4.7 (a)-(b) for both deflections.

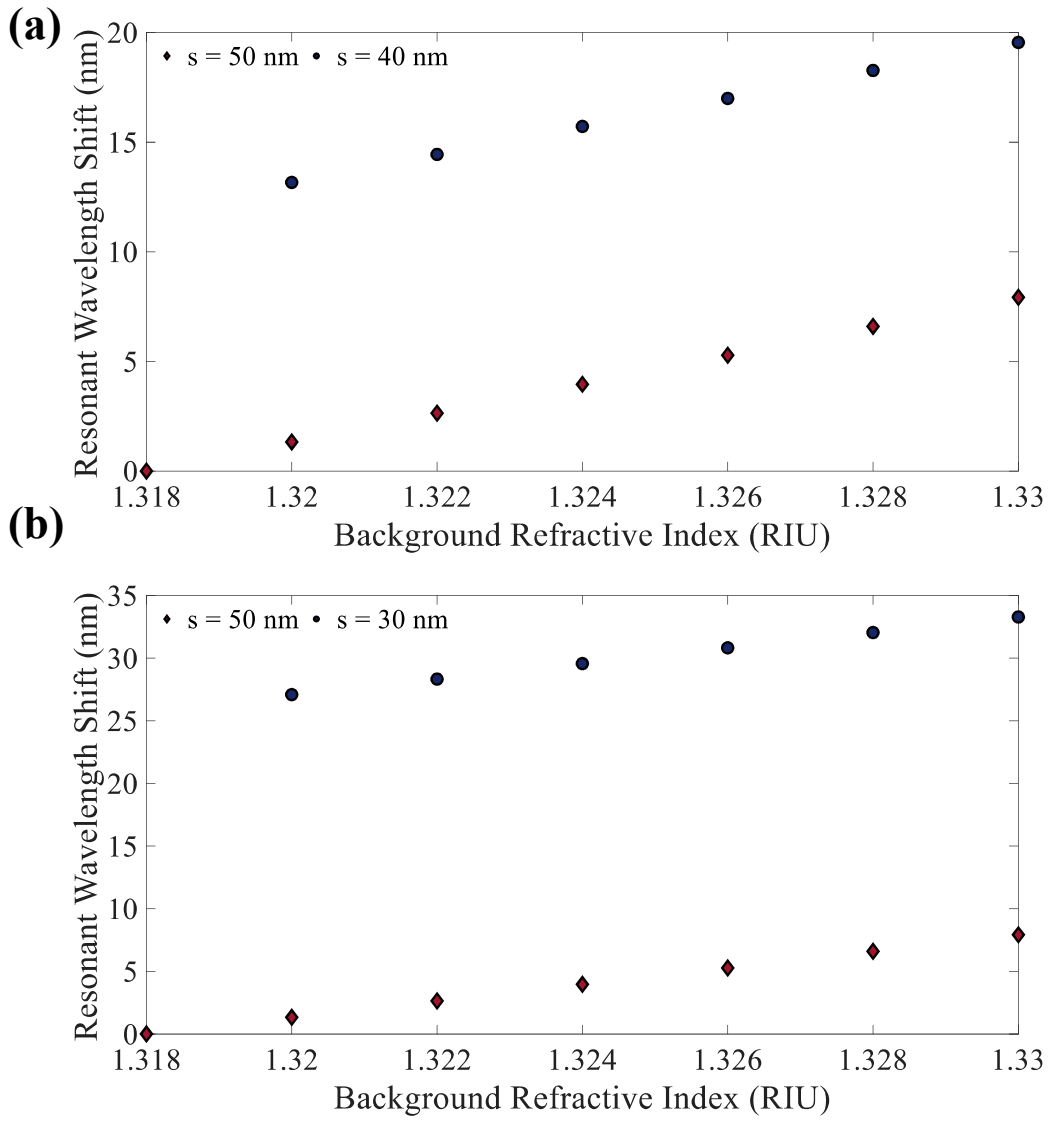

Figure 4.7 The presentation of the sensitivity enhancement for **(a)** 10 nm **(b)** 20 nm beam deflection.

The analysis of the sensitivity enhancement can be read by the plots in Figure 4.7(a)-(b), by observing the increase in the slope of the main line for certain background index value. The slope of the main line is 660 nm / RIU, which gives the intrinsic sensitivity of the bio-sensor. For instance, if the beam deflects for 10 nm for an index change of 0.012, the total combined resonant wavelength shift becomes 19.55 nm, corresponding to an enhanced sensitivity of 1629 nm/RIU. Therefore, more than

twofold enhancement occurs for such an operation. In order to fully extract the level of enhancement for different values of the background index change and slot width, we have tabulated the sensitivity values in Table 4.2.

Table 4.2 Sensitivity data for 10 nm and 20 nm deflection

Deflection (nm) / Δn_b (RIU)	*10*	*20*
0.002	6580 nm/RIU	13545 nm/RIU
0.004	3610 nm/RIU	7082 nm/RIU
0.006	2620 nm/RIU	4928 nm/RIU
0.008	2125 nm/RIU	3853 nm/RIU
0.010	1827 nm/RIU	3205 nm/RIU
0.012	1629 nm/RIU	2774 nm/RIU

Obviously, the sensitivity enhancement is maximized when the maximum amount of deflection can be triggered with a minimum amount of change in the background index. However, assuming large deflections with tiny variations in the background medium might not be practical. Our previous calculations maintain that 20 nm deflection is possible with a pump power of ~10 mW. Therefore, it is possible to enhance the sensitivity to a value of 2774 nm/RIU, for a change of 0.012 in the background medium, corresponding to an enhancement by a factor of 4.

In order to observe the effect of the initial slot width value, we also examined a cavity with an initial slot width of 100 nm. For this cavity, we again investigated the effect of 10 nm and 20 nm deflections, while the background index changes from 1.318 to 1.330. Increasing the initial width shifts the resonant wavelength to 1498 nm, while degrading the Q-factor to 1825 and increasing the sensitivity to 720 nm/RIU as a consequence of the trade-off that we mentioned earlier. The characteristics of the resonant wavelength with respect to the background refractive index are analyzed for the 10 nm and 20 nm deflection, and the data are tabulated in Table 4.3.

Table 4.3 Resonant wavelength characteristics of a cavity with an initial slot width of 100 nm for various n_b and s values

s (nm) / n_b *(RIU)*	*100*	*90*	*80*
1.318	1498.9 nm	1505.2 nm	1514.4 nm
1.320	1500.3 nm	1506.6 nm	1515.8 nm
1.322	1501.8 nm	1508.0 nm	1517.2 nm
1.324	1503.2 nm	1509.4 nm	1518.6 nm
1.326	1504.7 nm	1510.9 nm	1520.0 nm
1.328	1506.1 nm	1512.3 nm	1521.4 nm
1.330	1507.7 nm	1513.7 nm	1522.8 nm

By utilizing the data given in Table 4.3, we extracted the level of sensitivity enhancement for the beam deflections of 10 nm and 20 nm, respectively. Corresponding characteristics are plotted in Figure 4.8(a)-(b) for 10 nm and 20 nm beam deflections. For this configuration, the sensitivity is increased to 1234 nm/RIU for 10 nm slot width decrease, whereas the value of the sensitivity becomes 1989 nm/RIU for 20 nm beam deflection. Therefore, the optomechanical feedback loop enables almost threefold enhancement for the case of 20 nm deflection, with a background index change of 0.012.

In order to demonstrate the effect of the optomechanical feedback loop on the sensitivity of the bio-sensor in a better way, we also tabulated the sensitivity data for different values of deflection and background index change. Corresponding data are presented in Table 4.4. The data indicates that even if the initial slot width is increased to 100 nm, almost threefold enhancement of the sensitivity is possible, for a 0.012 background refractive index change and 20 nm slot width reduction.

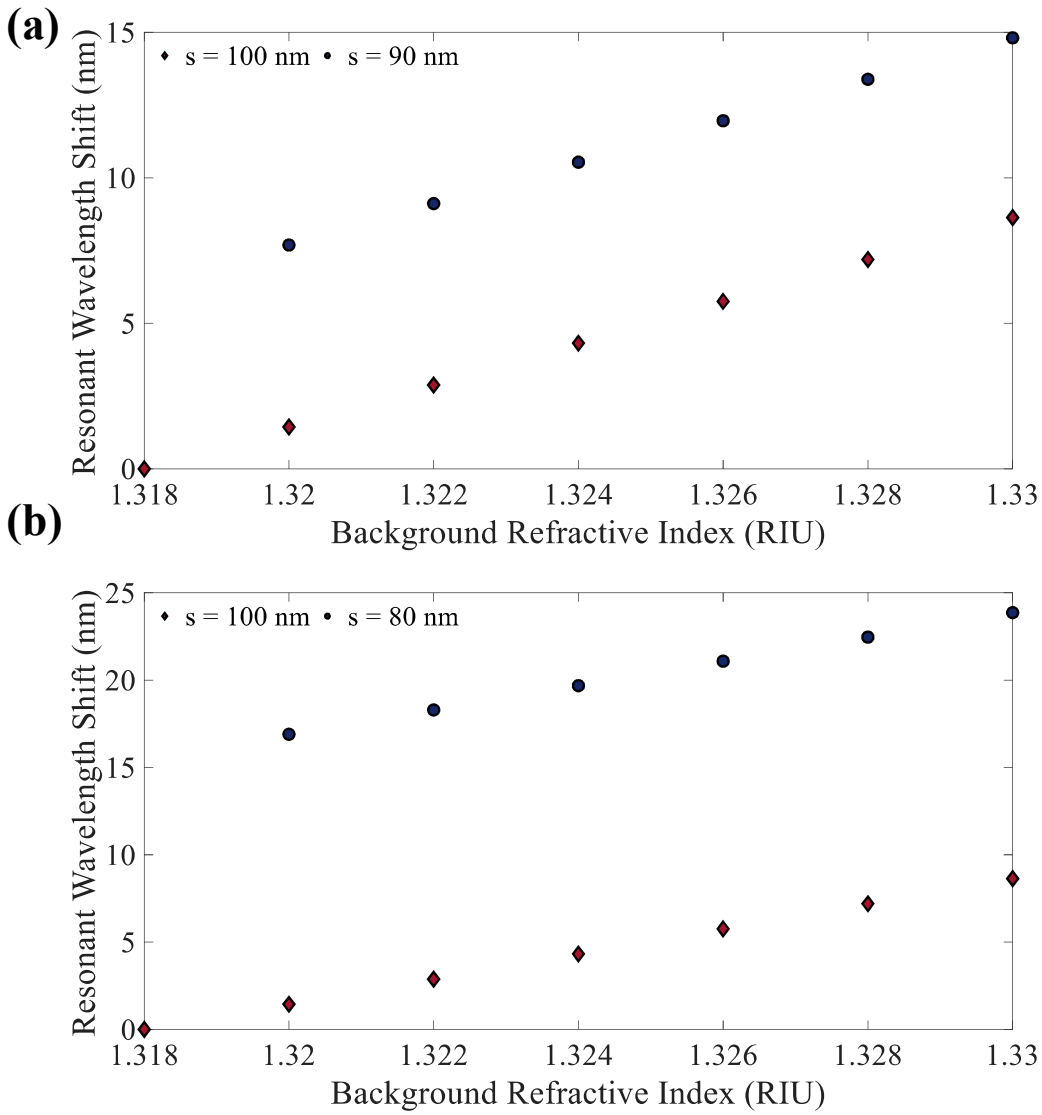

Figure 4.8 The presentation of the sensitivity enhancement of the cavity with an initial slot width of 100 nm for **(a)** 10 nm **(b)** 20 nm beam deflection.

Table 4.4 Sensitivity data of the cavity with the initial slot width of 100 nm for 10 nm and 20 nm deflection.

Deflection (nm) / Δn_b *(RIU)*	*10*	*20*
0.002	3846 nm/RIU	8450 nm/RIU
0.004	2278 nm/RIU	4573 nm/RIU

Table 4.4 (continued)

0.006	1757 nm/RIU	3280 nm/RIU
0.008	1495 nm/RIU	2636 nm/RIU
0.010	1339 nm/RIU	2246 nm/RIU
0.012	1234 nm/RIU	1989 nm/RIU

4.3.5 Q-factor Enhancement

The Q-factor of the cavity is also analyzed for different background index and slot width values in order to observe the effects of the optomechanical feedback on the Q-factor. Without the optomechanical feedback, the Q-factor of the cavity is decreased as t he intrusion of the analyte degrades the confinement strength of the cavity by decreasing the dielectric contrast between the cavity and the cladding. The optomechanical feedback compensates for the degradation since the slot width is also reduced during the operation. The Q-factor variation for an initial slot width of 50 nm is tabulated in Table 4.5.

Table 4.5 Q-factor characteristics of the cavity for different n_b and s values

s (nm) / n_b (RIU)	*50*	*40*	*30*
1.318	8262	11513	20620
1.320	7964	11324	20226
1.322	8110	11179	19913
1.324	7898	10947	19510
1.326	7764	10849	20102
1.328	7641	10590	19010
1.330	7523	10375	18651

The Q-factor characteristics depict that the decrease in the Q-factor can readily be compensated with the help of the optomechanical feedback. Notice that without the loop, the Q-factor goes down to 7723 as the background index changes to 1.330. By reducing the slot width by 20 nm, the Q-factor can reach up to 18651, corresponding to an approximately twofold enhancement. The enhancement of the Q-factor for different background index shifts and beam deflections is presented in Figure 4.9.

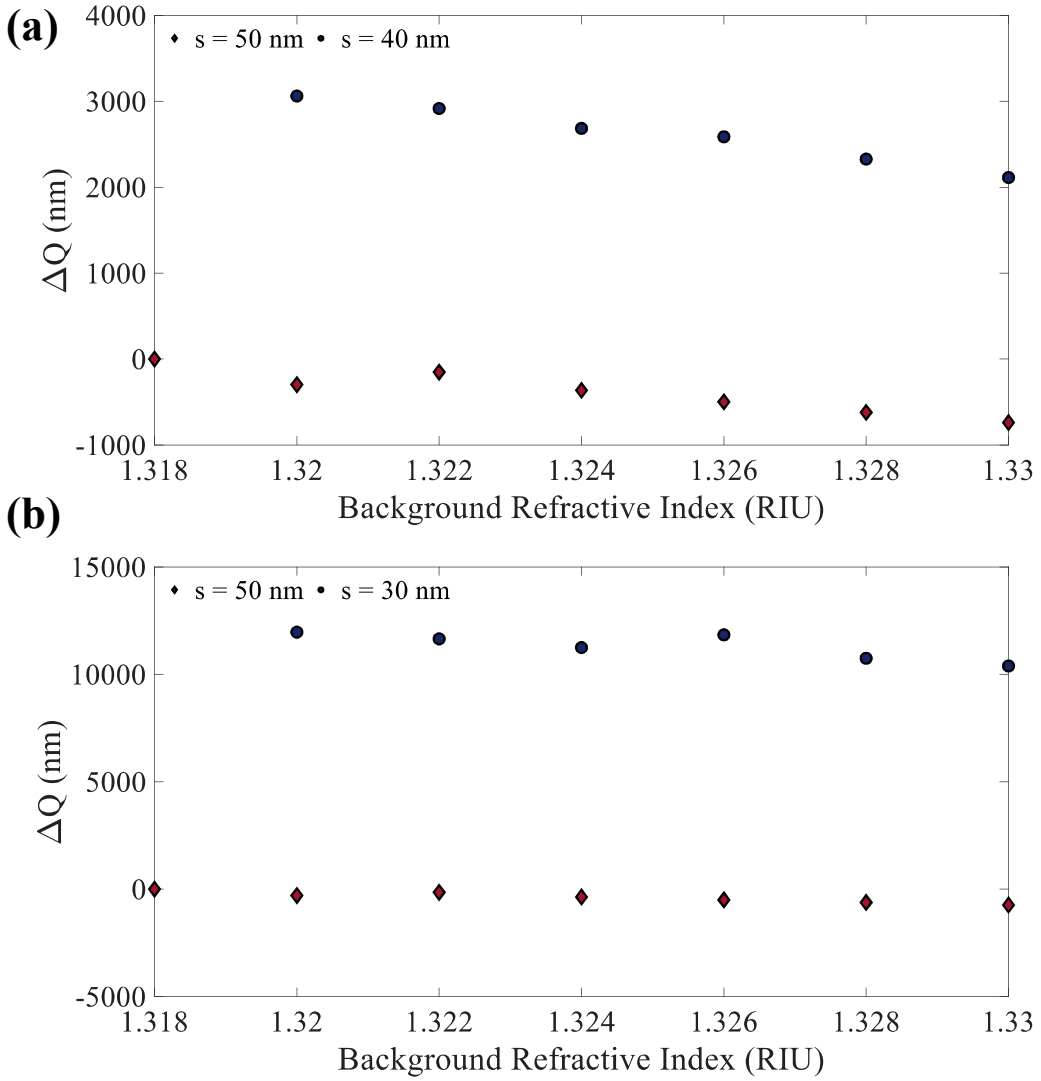

Figure 4.9 The presentation of the Q-factor enhancement of the cavity with an initial slot width of 50 nm for **(a)** 10 nm **(b)** 20 nm beam deflection.

Additionally, the effect of the optomechanical enhancement on the Q-factor of the cavity is also analyzed for the case of 100 nm initial slot width, and it is tabulated in Table 4.6.

Table 4.6 Q-factor characteristics of the cavity for different n_b and s values.

s (nm) / n_b (RIU)	*100*	*90*	*80*
1.318	1825	2085	2268
1.320	1804	2059	2138
1.322	1784	2035	2217
1.324	1763	2014	2191
1.326	1745	1986	2133
1.328	1722	1968	2142
1.330	1703	1943	2073

The Q-factor of the cavity with an initial slot width of 100 nm is 1825 when there is no optomechanical effect. For a 20 nm slot width reduction, the Q-factor degradation is totally compensated, and it is even enhanced to 2073 when the background refractive index increased by 0.012. Therefore, even when the slot width is increased, the optomechanical feedback loop is able to enhance both of the performance factors at the same time. The level of compensation and enhancement of the Q-factor are given in Figure 4.10(a)-(b) for different values of background refractive index and slot width.

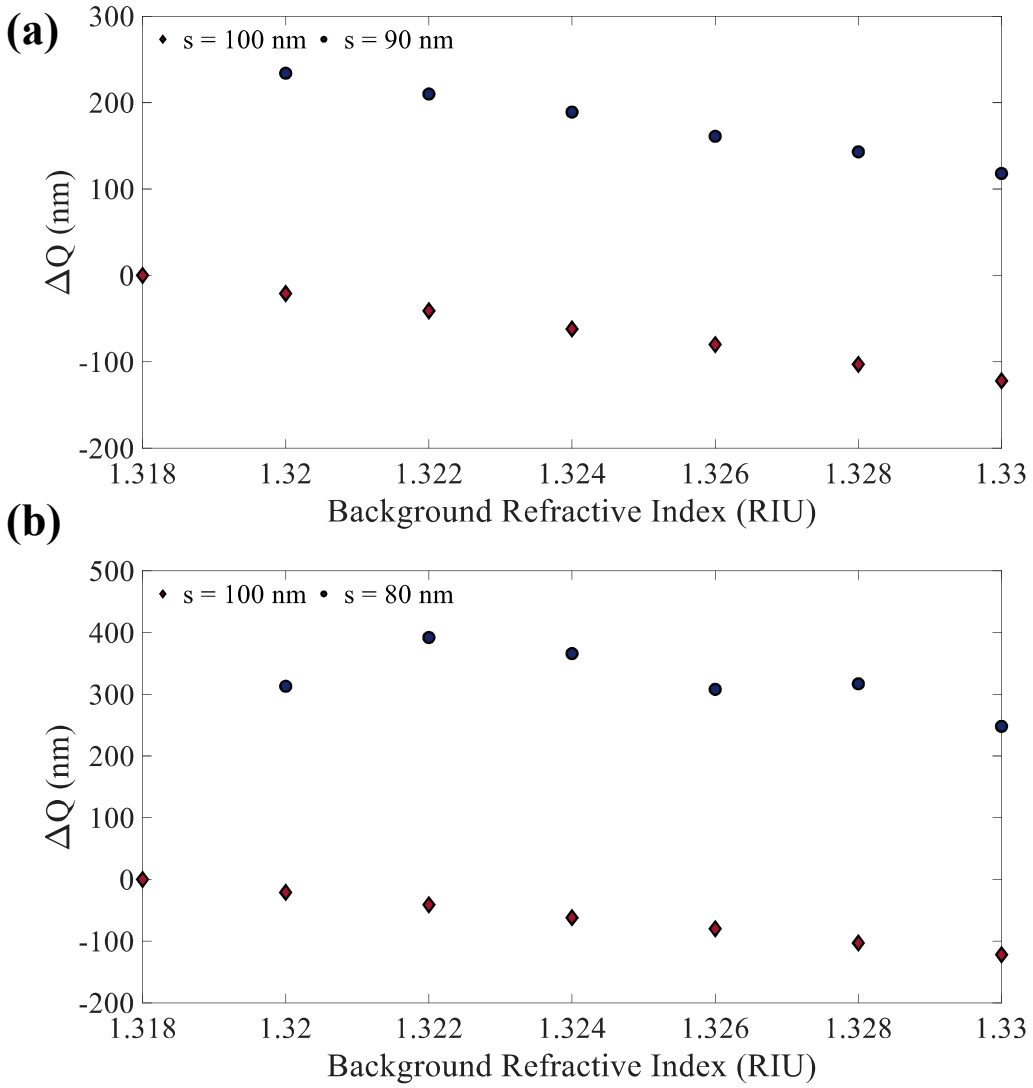

Figure 4.10 The presentation of the Q-factor enhancement of the cavity with an initial slot width of 100 nm for **(a)** 10 nm **(b)** 20 nm beam deflection.

CHAPTER 5

CONCLUSION AND FUTURE WORK

In this thesis, we demonstrated an optically resonant structure to be utilized for refractive index based optical bio-sensing purposes, constructed by utilizing a 1D slot mode PhC nanobeam cavity. We enhanced the refractive index sensing performance by implementing an optomechanical feedback loop generating optical transverse gradient forces inside the cavity. The generated forces modify the width of the slot in accordance with the presence of the target analyte in the background medium. When this is the case, the performance factors, namely Q-factor and sensitivity, of the bio-sensor can be increased together, resulting in the elimination of a trade-off, intrinsically present in the slotted resonant cavity bio-sensing mechanisms. Throughout the thesis, we directed our focus mostly on the investigation of the device performance in terms of the quantification of the response of the optical system to background refractive index changes and the enhancement characteristics of the applied optomechanical feedback via various numerical analyses and provided the corresponding results. Based on the results, we are able to enhance the sensitivity of the device by a factor of four, without sacrificing from the Q-factor at all. In fact, we even saw a twofold improvement in the Q-factor, too.

Refractive index based optical bio-sensing mechanisms have been getting larger attention due to the advantages they offer. Especially, label-free sensing is highly important, as it significantly lowers the operation complexity [28]. Resonant structures are perfectly suitable for optical bio-sensing applications since they can provide label-free sensing by their strong light confinement capability [5], [28], [39], [84]. Among them, 1D slotted PhC nanobeam cavities possess the ability to confine the light in extremely small volumes. For the purpose of eminent performance, the researchers have been focusing on the methodology of the design of 1D slotted PhC nanobeam cavities. Extensive parameter search is the most common method on the

determination of the device geometry and material properties [76], [77], [81]. However, such a method requires exhaustive effort and computational cost. Our enhancement method removes the necessity of such an effort due to the dynamic device functionality. Moreover, the operation principle of the appended optomechanical feedback loop is not limited by a certain type of optical bio-sensor, and it can be readily appended to any resonant structure, used for optical bio-sensing purposes. Therefore, the utilization of such a method on the state-of-the-art refractive index based optical bio-sensing configurations may lead to promising results and might further push the limits on the detection of tiny single nanoparticles and other types of analytes of interest.

From the structural point of view, the study performed in this thesis enlightens the theory and the analytical background of the proposed structure and supports the proposed idea with various numerical analyses. Currently, the study is in the fabrication phase, where we work on the implementation of the slotted 1D PhC nanobeam cavities. During this phase, the main difficulty that we have encountered is to proper implementation of the suspended slotted structure without the nanobeams sticking to each other. The inherent large aspect-ratio of the structure, combined with the small feature size of the slot, makes the device susceptible to the tiny variations in the fabrication process. Furthermore, since the slot divides the structure into two independent, long, and thin beams, the possible buckling of the beams might harden the fabrication and cause performance degradation, requiring an exhausting optimization process. After overcoming these steps, our aim will, obviously, be to experimentally characterize the device performance and the enhancement via optomechanical feedback loop.

REFERENCES

[1] K. Yin, "Design of Novel Biosensors for Optical Sensing and Their Applications in Environmental Analysis," Chinese Academy of Sciences, 2018.

[2] I. Abdulhalim, M. Zourob, and A. Lakhtakia, "Overview of Optical Biosensing Techniques," *Handb. Biosens. Biochips*, 2008.

[3] J. Kim, A. S. Campbell, B. E. F. de Ávila, and J. Wang, "Wearable biosensors for healthcare monitoring," *Nat. Biotechnol.*, vol. 37, no. 4, pp. 389–406, 2019.

[4] R. Méjard, H. J. Griesser, and B. Thierry, "Optical biosensing for label-free cellular studies," *TrAC - Trends Anal. Chem.*, vol. 53, pp. 178–186, 2013.

[5] P. Moock *et al.*, "TDM-controlled ring resonator arrays for fast, fixed-wavelength optical biosensing," *Opt. Express*, vol. 26, no. 17, p. 22356, 2018.

[6] E. Morales-Narváez and A. Merkoçi, "Graphene Oxide as an Optical Biosensing Platform: A Progress Report," *Adv. Mater.*, vol. 31, no. 6, pp. 1–12, 2019.

[7] C. Wu *et al.*, "Fano-resonant asymmetric metamaterials for ultrasensitive spectroscopy and identification of molecular monolayers," *Nat. Mater.*, vol. 11, no. 1, pp. 69–75, 2012.

[8] M. D. Baaske, M. R. Foreman, and F. Vollmer, "Single-molecule nucleic acid interactions monitored on a label-free microcavity biosensor platform," *Nat. Nanotechnol.*, vol. 9, no. 11, pp. 933–939, 2014.

[9] D.-X. Xu *et al.*, "Label-free biosensor array based on silicon-on-insulator ring resonators addressed using a WDM approach," *Opt. Lett.*, vol. 35, no. 16, p. 2771, 2010.

[10] S. Lee, S. C. Eom, J. S. Chang, J. H. Shin, G. Y. Sung, and C. Huh, "Label-free optical biosensing using a horizontal air-slot SiNx microdisk resonator," *Opt. Express*, vol. 18, no. 20, pp. 258–259, 2010.

[11] F. Yesilkoy *et al.*, “Ultrasensitive hyperspectral imaging and biodetection enabled by dielectric metasurfaces,” *Nat. Photonics*, vol. 13, no. 6, pp. 390–396, 2019.

[12] M. Erdil, Y. Ozer, and S. Kocaman, “High-Q slot-mode photonic crystal nanobeam cavity biosensor with optomechanically enhanced sensitivity,” *IEEE J. Sel. Top. Quantum Electron.*, vol. 25, no. 2, pp. 1–6, 2019.

[13] M. Piliarik and V. Sandoghdar, “Direct optical sensing of single unlabelled proteins and super-resolution imaging of their binding sites,” *Nat. Commun.*, vol. 5, pp. 1–8, 2014.

[14] S. Kita *et al.*, “Super-sensitivity in label-free protein sensing using a nanoslot nanolaser,” *Opt. Express*, vol. 19, no. 18, p. 17683, 2011.

[15] S. Liakat, K. A. Bors, L. Xu, C. M. Woods, J. Doyle, and C. F. Gmachl, “Noninvasive in vivo glucose sensing on human subjects using mid-infrared light,” *Biomed. Opt. Express*, vol. 5, no. 7, p. 2397, 2014.

[16] B. J. Vakoc, D. Fukumura, R. K. Jain, and B. E. Bouma, “Cancer imaging by optical coherence tomography: Preclinical progress and clinical potential,” *Nat. Rev. Cancer*, vol. 12, no. 5, pp. 363–368, 2012.

[17] J. Witt *et al.*, “Medical textiles with embedded fiber optic sensors for monitoring of respiratory movement,” *IEEE Sens. J.*, vol. 12, no. 1, pp. 246–254, 2012.

[18] T. Hara, A. Mentbayeva, and A. Konarov, “Systems and Methods for Monitoring Brain Metabolism and Activity Using Electroencephalogram and Optical Imaging,” 2014.

[19] N. M. Iverson *et al.*, “In vivo biosensing via tissue-localizable near-infrared-fluorescent single-walled carbon nanotubes,” *Nat. Nanotechnol.*, vol. 8, no. 11, pp. 873–880, 2013.

[20] L. Lan, Y. Yao, J. Ping, and Y. Ying, “Recent advances in nanomaterial-based biosensors for antibiotics detection,” *Biosens. Bioelectron.*, vol. 91, no.

October 2016, pp. 504–514, 2017.

[21] S. Kaushik, U. K. Tiwari, A. Deep, and R. K. Sinha, “Two-dimensional transition metal dichalcogenides assisted biofunctionalized optical fiber SPR biosensor for efficient and rapid detection of bovine serum albumin,” *Sci. Rep.*, vol. 9, no. 1, pp. 1–11, 2019.

[22] P. Singh, “SPR Biosensors: Historical Perspectives and Current Challenges,” *Sensors Actuators, B Chem.*, vol. 229, pp. 110–130, 2016.

[23] M. Bauch and J. Dostalek, “Collective localized surface plasmons for high performance fluorescence biosensing,” *Opt. Express*, vol. 21, no. 17, p. 20470, 2013.

[24] F. S. Ligler and C. R. Taitt, *Optical Biosensors: Today and Tomorrow*, 2nd ed. 2008.

[25] F. Mitschke, *Fiber optics: Physics and technology*, 2nd ed. 2016.

[26] C. R. Pollock and M. Lipson, *Integrated Photonics*. 2003.

[27] M. Erdil and S. Kocaman, “Breaking the trade-off between sensitivity and Q-factor for high-Q slot mode photonic crystal nanobeam cavity biosensors with optomechanical feedback,” in *Proc. SPIE 10875, Microfluidics, BioMEMS, and Medical Microsystems XVII*, 2019.

[28] F. Carpignano, G. Rigamonti, T. Migliazza, and S. Merlo, “Refractive Index Sensing in Rectangular Glass Micro-Capillaries by Spectral Reflectivity Measurements,” *IEEE J. Sel. Top. Quantum Electron.*, vol. 22, no. 3, 2016.

[29] G. Li, Y. Shen, G. Xiao, and C. Jin, “Double-layered metal grating for high-performance refractive index sensing,” *Opt. Express*, vol. 23, no. 7, p. 8995, 2015.

[30] Y. Shen *et al.*, “Plasmonic gold mushroom arrays with refractive index sensing figures of merit approaching the theoretical limit,” *Nat. Commun.*, vol. 4, 2013.

[31] P. Xu, K. Yao, J. Zheng, X. Guan, and Y. Shi, “Slotted photonic crystal

nanobeam cavity with parabolic modulated width stack for refractive index sensing," *Opt. Express*, vol. 21, no. 22, p. 26908, 2013.

[32] Y. Guo, H. Li, K. Reddy, H. S. Shelar, V. R. Nittoor, and X. Fan, "Optofluidic Fabry-Pérot cavity biosensor with integrated flow-through micro-/nanochannels," *Appl. Phys. Lett.*, vol. 98, no. 4, pp. 10–13, 2011.

[33] J. Tian, Y. Lu, Q. Zhang, and M. Han, "Microfluidic refractive index sensor based on an all-silica in-line Fabry–Perot interferometer fabricated with microstructured fibers," *Opt. Express*, vol. 21, no. 5, p. 6633, 2013.

[34] I. Brice *et al.*, "Development of optical WGM resonators for biosensors," in *Proc. SPIE 10592, Biophotonics*, 2017.

[35] J. Li, R. Yu, C. Ding, and Y. Wu, "PT-symmetry-induced evolution of sharp asymmetric line shapes and high-sensitivity refractive index sensors in a three-cavity array," *Phys. Rev. A*, vol. 93, no. 2, pp. 1–8, 2016.

[36] B. Su, C. Wang, Q. Kan, and H. Chen, "Compact silicon-on-insulator dual-microring resonator optimized for sensing," *J. Light. Technol.*, vol. 29, no. 10, pp. 1535–1541, 2011.

[37] K. Qin, S. Hu, S. T. Retterer, I. I. Kravchenko, and S. M. Weiss, "Slow light Mach–Zehnder interferometer as label-free biosensor with scalable sensitivity," *Opt. Lett.*, vol. 41, no. 4, pp. 753–756, 2016.

[38] Y. Gao, P. Dong, and Y. Shi, "Suspended slotted photonic crystal cavities for high-sensitivity refractive index sensing," *Opt. Express*, vol. 28, no. 8, p. 12272, 2020.

[39] S. Pal, E. Guillermain, R. Sriram, B. L. Miller, and P. M. Fauchet, "Silicon photonic crystal nanocavity-coupled waveguides for error-corrected optical biosensing," *Biosens. Bioelectron.*, vol. 26, no. 10, pp. 4024–4031, 2011.

[40] D. Yang, C. Wang, and Y. Ji, "Silicon on-chip 1D photonic crystal nanobeam bandstop filters for the parallel multiplexing of ultra-compact integrated 1d photonic crystal nanobeam cavity sensors array," *Opt. Express*, vol. 24, no.

15, pp. 16267–16279, 2016.

[41] C. Wang, Q. Quan, S. Kita, Y. Li, and M. Lončar, “Single-nanoparticle detection with slot-mode photonic crystal cavities,” *Appl. Phys. Lett.*, vol. 106, no. 26, 2015.

[42] D. K. Cheng, *Fundamentals of Engineering Electromagnetics*. 1993.

[43] J. D. Joannopoulos, S. G. Johnson, J. N. Winn, and R. D. Meade, *Photonic Crystals: Molding the Flow of Light*, 2nd ed. 2008.

[44] J. D. Joannopoulos, P. R. Villeneuve, and S. Fan, “Photonic crystals: putting a new twist on light,” *Nature*, vol. 386, no. 6621, pp. 143–149, 1997.

[45] S. John, “Strong localization of photons in certain disordered dielectric superlattices,” *Phys. Rev. Lett.*, vol. 58, no. 23, pp. 2486–2489, 1987.

[46] E. Yablonovitch, “Inhibited Spontaneous Emission in Solid-State Physics and Electronics,” *Phys. Rev. Lett.*, vol. 58, no. 20, pp. 2059–2062, 1987.

[47] T. Baba, “Slow light in photonic crystals,” *Nat. Photonics*, vol. 2, no. 8, pp. 465–473, 2008.

[48] N. Segal, S. Keren-Zur, N. Hendler, and T. Ellenbogen, “Controlling light with metamaterial-based nonlinear photonic crystals,” *Nat. Photonics*, vol. 9, no. 3, pp. 180–184, 2015.

[49] S. Kocaman *et al.*, “Zero phase delay in negative-refractive-index photonic crystal superlattices,” *Nat. Photonics*, vol. 5, no. 8, pp. 499–505, 2011.

[50] A. Di Falco, L. O’Faolain, and T. F. Krauss, “Photonic crystal slotted slab waveguides,” *Photonics Nanostructures - Fundam. Appl.*, vol. 6, no. 1, pp. 38–41, 2008.

[51] S. Johnson and J. Joannopoulos, “Block-iterative frequency-domain methods for Maxwell’s equations in a planewave basis,” *Opt. Express*, vol. 8, no. 3, p. 173, 2001.

[52] A. Govdeli, M. C. Sarihan, U. Karaca, and S. Kocaman, “Integrated Optical

Modulator Based on Transition between Photonic Bands," *Sci. Rep.*, vol. 8, no. 1, pp. 1–11, 2018.

[53] M. Erdil and S. Kocaman, "Optomechanically Enhanced High-Q Slot Mode Photonic Crystal Nanobeam Cavity," in *31st Annual Conference of the IEEE Photonics Society, IPC*, 2018, pp. 31–32.

[54] Q. Quan and M. Loncar, "Deterministic design of wavelength scale, ultra-high Q photonic crystal nanobeam cavities," *Opt. Express*, vol. 19, no. 19, pp. 18529–18542, 2011.

[55] M. J. Burek *et al.*, "High quality-factor optical nanocavities in bulk single-crystal diamond," *Nat. Commun.*, vol. 5, no. May, pp. 1–7, 2014.

[56] Y. Zhang and Y. Shi, "Post-trimming of photonic crystal nanobeam cavities by controlled electron beam exposure," *Opt. Express*, vol. 24, no. 12, p. 12542, 2016.

[57] A. Govdeli and S. Kocaman, "On-Chip Switch and Add/Drop Multiplexer Design with Left-Handed Behavior in Photonic Crystals," *IEEE J. Sel. Top. Quantum Electron.*, vol. 26, no. 2, 2020.

[58] N. H. Wan, S. Mouradian, and D. Englund, "Two-dimensional photonic crystal slab nanocavities on bulk single-crystal diamond," *Appl. Phys. Lett.*, vol. 112, no. 14, pp. 3–7, 2018.

[59] K. Svoboda and S. M. Block, "Biological applications of optical forces," *Annu. Rev. Biophys. Biomol. Struct.*, vol. 23, pp. 247–285, 1994.

[60] J. Chen, J. Ng, Z. Lin, and C. T. Chan, "Optical pulling force," *Nat. Photonics*, vol. 5, no. 9, pp. 531–534, 2011.

[61] D. Van Thourhout and J. Roels, "Optomechanical device actuation through the optical gradient force," *Nat. Photonics*, vol. 4, no. 4, pp. 211–217, 2010.

[62] Y. Ozer and S. Kocaman, "Stability Formulation for Integrated Opto-mechanic Phase Shifters," *Sci. Rep.*, vol. 8, no. 1937, pp. 1–9, 2018.

[63] M. Aspelmeyer, T. J. Kippenberg, and F. Marquardt, "Cavity

optomechanics," *Rev. Mod. Phys.*, vol. 86, no. 4, pp. 1391–1452, 2014.

[64] A. N. Grigorenko, N. W. Roberts, M. R. Dickinson, and Y. Zhang, "Nanometric optical tweezers based on nanostructured substrates," *Nat. Photonics*, vol. 2, no. 6, pp. 365–370, 2008.

[65] F. Benz *et al.*, "Single-molecule optomechanics in 'picocavities,'" *Science (80-.).*, vol. 354, no. 6313, pp. 726–729, 2016.

[66] S. Divitt, L. Rondin, and L. Novotny, "Cancellation of non-conservative scattering forces in optical traps by counter-propagating beams," *Opt. Lett.*, vol. 40, no. 9, p. 1900, 2015.

[67] S. Kar *et al.*, "Ion acceleration in multispecies targets driven by intense laser radiation pressure," *Phys. Rev. Lett.*, vol. 109, no. 18, pp. 1–5, 2012.

[68] M. C. Frawley, I. Gusachenko, V. G. Truong, M. Sergides, and S. N. Chormaic, "Selective particle trapping and optical binding in the evanescent field of an optical nanofiber," vol. 22, no. 13, pp. 16322–16334, 2014.

[69] M. L. Povinelli *et al.*, "Evanescent-wave bonding between optical waveguides," *Opt. Lett.*, vol. 30, no. 22, p. 3042, 2005.

[70] W. H. P. Pernice, M. Li, K. Y. Fong, and H. X. Tang, "Modeling of the optical force between propagating lightwaves in parallel 3D waveguides," *Opt. Express*, vol. 17, no. 18, p. 16032, 2009.

[71] A. Pontin *et al.*, "Squeezing a thermal mechanical oscillator by stabilized parametric effect on the optical spring," *Phys. Rev. Lett.*, vol. 112, no. 2, pp. 1–5, 2014.

[72] Y. C. Liu, Y. W. Hu, C. W. Wong, and Y. F. Xiao, "Review of cavity optomechanical cooling," *Chinese Phys. B*, vol. 22, no. 11, 2013.

[73] G. A. T. Pender, P. F. Barker, F. Marquardt, J. Millen, and T. S. Monteiro, "Optomechanical cooling of levitated spheres with doubly resonant fields," *Phys. Rev. A*, vol. 85, no. 2, pp. 3–6, 2012.

[74] A. Nunnenkamp, V. Sudhir, A. K. Feofanov, A. Roulet, and T. J. Kippenberg,

"Quantum-limited amplification and parametric instability in the reversed dissipation regime of cavity optomechanics," *Phys. Rev. Lett.*, vol. 113, no. 2, pp. 1–5, 2014.

[75] V. R. Almeida, Q. Xu, C. A. Barrios, and M. Lipson, "Guiding and confining light in void nanostructure," *Opt. Lett.*, vol. 29, no. 11, pp. 1209–1211, 2004.

[76] T. Li, D. Gao, D. Zhang, and E. Cassan, "High- Q and High-Sensitivity One-Dimensional Photonic Crystal Nanobeam Cavity Sensors," vol. 28, no. 6, pp. 689–692, 2016.

[77] D. Yang, H. Tian, and Y. Ji, "High-Q and high-sensitivity width-modulated photonic crystal single nanobeam air-mode cavity for refractive index sensing," *Appl. Opt.*, vol. 54, no. 1, p. 1, 2015.

[78] C. Y. Kao and F. Santosa, "Maximization of the quality factor of an optical resonator," *Wave Motion*, vol. 45, no. 4, pp. 412–427, 2008.

[79] Y. N. Zhang, Y. Zhao, and R. Q. Lv, "A review for optical sensors based on photonic crystal cavities," *Sensors Actuators, A Phys.*, vol. 233, pp. 374–389, 2015.

[80] P. T. Kristensen, C. Van Vlack, and S. Hughes, "Generalized effective mode volume for leaky optical cavities," *Opt. Lett.*, vol. 37, no. 10, pp. 1649–1651, 2012.

[81] D. Yang, P. Zhang, H. Tian, Y. Ji, and Q. Quan, "Ultrahigh-Q and low-mode-volume parabolic radius-modulated single photonic crystal slot nanobeam cavity for high-sensitivity refractive index sensing," *IEEE Photonics J.*, vol. 7, no. 5, 2015.

[82] Q. Quan, P. B. Deotare, and M. Loncar, "Photonic crystal nanobeam cavity strongly coupled to the feeding waveguide," *Appl. Phys. Lett.*, vol. 96, no. 20, pp. 94–97, 2010.

[83] A. F. Oskooi, D. Roundy, M. Ibanescu, P. Bermel, J. D. Joannopoulos, and S. G. Johnson, "Meep: A flexible free-software package for electromagnetic

simulations by the FDTD method," *Comput. Phys. Commun.*, vol. 181, no. 3, pp. 687–702, 2010.

[84] Q. Quan *et al.*, "Single particle detection in CMOS compatible photonic crystal nanobeam cavities," *Opt. Express*, vol. 21, no. 26, p. 32225, 2013.

APPENDICES

A. Photonic Band Diagram Extraction

```
; Mertcan Erdil METU EEE 2020


(set-param! resolution 32)        ; simulation cell resolution

; parameter definition

(define-param a 0.48)                     ; lattice constant
(define-param h 0.220)            ; nanobeam thickness
(define-param w 0.67)                     ; nanobeam width
(define-param s 0.05)                     ; slot width
(define-param r 0.220)            ; hole radius

(define-param nSi 3.48)           ; Si refractive index
(define-param nC 1.318)   ; background refractive index


; normalization of geometry parameters w.r.t. lattice constant

(set! r (/ r a))
(set! h (/ h a))
(set! w (/ w a))
(set! s (/ s a))

; background media definition
(set! default-material (make dielectric (index nC)))


; simulation cell definition

(set! geometry-lattice (make lattice (size 1 4 4)))


; unit cell geometry definition

(set! geometry (list
  (make block (center 0 0 0) (size infinity w h) (material (make
dielectric (index nSi))))
  (make cylinder (center 0 0 0) (radius r) (height infinity) (material
(make dielectric (index nC))))
  (make block (center 0 0 0) (size infinity s h) (material (make
dielectric (index nC))))))

; definition of k vector array
```

```
45
46 (set! k-points (list (vector3 0 0 0) (vector3 0.5 0 0)))
47 (define-param num-kpoints 20)
48 (set! k-points (interpolate num-kpoints k-points))
49
50 (set-param! num-bands 2); number of bands to be extracted
51
52 (run-yodd-zeven)
```

B. Resonant Mode Analysis

```
; Mertcan Erdil EEE 2020

(set! resolution 40); simulation cell resolution, a = 480

; geometry parameter definition (normalized by a)
(define-param w 1.3958)        ; nanobeam width
(define-param t 0.4583)        ; nanobeam thickness
(define-param dair 2)          ; air clad thickness
(define-param dpml 2)          ; PML layer thickness
(define-param pad 1)           ; padding length
(define-param s 0.1042)
(define-param rcen 0.4583); radius of the center hole
(define-param rend 0.3958)     ; radius of the last mirror
segment

(define-param Ndef_taper 15); number of tapered mirror segments
at one side

(define-param Ndef_end 0); number of additional mirror segments


; simulation cell generation
(define sx (* (+ Ndef_taper Ndef_end 1 dpml pad) 2))
(define sy (+ dpml dair w dair dpml))
(define sz (+ dpml dair t dair dpml))
(set! geometry-lattice (make lattice (size sx sy sz)))


; PML generation
(set! pml-layers (list (make pml (thickness dpml))))


; material parameters
(define-param nSi 3.48)        ; Si refractive index
(define-param nC  1.318 )      ; background refractive index
(set! default-material (make dielectric (index nC)))

; geometry generation
(set! geometry (list (make block (center 0 0 0) (size infinity
w t) (material (make dielectric (index nSi))))
                     (make block (center 0 0 0) (size
infinity s t) (material (make dielectric (index nC))))
))

(define holes (list '()))
(set! holes (append holes
```

```
47 (map (lambda (mm) (list
48                 (make cylinder (center (- +0.5 mm) 0 0) (radius
49 (+ rcen (/ (* (- mm 1) (- mm 1) (- rend rcen)) 196))) (height
50 infinity) (material (make dielectric (index nC))))
51                 (make cylinder (center (+ -0.5 mm) 0 0) (radius
52 (+ rcen (/ (* (- mm 1) (- mm 1) (- rend rcen)) 196))) (height
53 infinity) (material (make dielectric (index nC))))))
54         (arith-sequence 1 1  Ndef_taper))
55 (map (lambda (nn) (list
56                 (make cylinder (center (- +0.5 nn) 0 0) (radius
57 rend) (height infinity) (material (make dielectric (index
58 nC))))
59                 (make cylinder (center (+ -0.5 nn) 0 0) (radius
60 rend) (height infinity) (material (make dielectric (index
61 nC))))))
62         (arith-sequence 31 1 Ndef_end))
63
64 ))
65 (set! holes (apply append holes))
66 (set! geometry (append geometry holes))
67
68 ; spectral parameters
69 (define-param fcen 0.298)      ; center frequency of the source
70 (define-param df 0.01) ; spectral width of the source
71
72 ;definition of the Gaussian source
73 (set! sources (list (make source
74         (src (make gaussian-src (frequency fcen) (fwidth df)))
75         (component Ey) (center 0 0 0) )))

  ; symmetry settings
  (set! symmetries (list
          (make mirror-sym (direction X) (phase +1))
          (make mirror-sym (direction Y) (phase -1))
    (make mirror-sym (direction Z) (phase +1))))

  ; simulation run
  (run-sources+ 800
          (at-beginning output-epsilon)
          (after-sources (harminv Ey (vector3 0 0 0) fcen df))
          (in-volume (volume (center 0 0 0) (size sx sy 0))(at-end
  output-efield-y)))
```

C. Transmission Spectrum Analysis

```
; Mertcan Erdil METU EEE 2020

(set! resolution 40)  ; simulation cell resolution, a =480 nm

;geometry parameters (normalized by a)
(define-param w 1.3958)        ; nanobeam width
(define-param t 0.4583)        ; nanobeam thickness
(define-param dair 1.5)        ; cladding thickness
(define-param dpml 1.5)        ; PML thickness
(define-param pad 1)           ; padding length
(define-param s 0.1042)        ; slot width
(define-param rcen 0.4583)     ; center hole radius
(define-param rend 0.3958) ; end hole radius

(define-param Ndef_taper 15)   ; number of tapered mirror
segments
(define-param Ndef_end 0)      ; number of additional mirror
segments

; simulation environment generation
(define sx (* (+ Ndef_taper Ndef_end 1 dpml pad) 2))
(define sy (+ dpml dair w dair dpml))
(define sz (+ dpml dair t dair dpml))
(set! geometry-lattice (make lattice (size sx sy sz)))

;PML settings
(set! pml-layers (list (make pml (thickness dpml))))

;material parameters
(define-param nSi 3.48)        ;Si refractive index
(define-param nC  1.318 ) ;background refractive index (water)
(set! default-material (make dielectric (index nC)))

; generation of geometry
(set! geometry (list (make block (center 0 0 0) (size infinity
w t) (material (make dielectric (index nSi))))
                     (make block (center 0 0 0) (size
infinity s t) (material (make dielectric (index nC))))
))

(define holes (list '()))
(set! holes (append holes
        (map (lambda (mm) (list
                (make cylinder (center (- +0.5 mm) 0 0) (radius
(+ rcen (/ (* (- mm 1) (- mm 1) (- rend rcen)) 196))) (height
infinity) (material (make dielectric (index nC))))
```

```
47                (make cylinder (center (+ -0.5 mm) 0 0) (radius
48 (+ rcen (/ (* (- mm 1) (- mm 1) (- rend rcen)) 196))) (height
49 infinity) (material (make dielectric (index nC))))))
50         (arith-sequence 1 1  Ndef_taper))
51 (map (lambda (nn) (list
52                (make cylinder (center (- +0.5 nn) 0 0) (radius
53 rend) (height infinity) (material (make dielectric (index
54 nC))))
55                (make cylinder (center (+ -0.5 nn) 0 0) (radius
56 rend) (height infinity) (material (make dielectric (index
57 nC))))))
58         (arith-sequence 31 1 Ndef_end))
59
60 ))
61 (set! holes (apply append holes))
62 (set! geometry (append geometry holes))
63
64 ;spectral parameters
65 (define-param fcen 0.3108)     ; center frequency
66 (define-param df 0.08) ; spectral width of the source
67 (define-param nfreq 32768)     ; number of FFT points
68
69 ; generation of Gaussian source
70 (set! sources (list (make source
71         (src (make gaussian-src (frequency fcen) (fwidth df)))
72         (component Ey) (center (+ (* -0.5 sx) dpml 1) 0 0) (size
73 0 w t))))
74
75 ;symmetry settings
76 (set! symmetries (list
77         (make mirror-sym (direction Y) (phase -1))
78         (make mirror-sym (direction Z) (phase +1))))
79
80
   (define trans ; transmitted flux
           (add-flux fcen df nfreq
                     (make flux-region
                       (center (- (* 0.5 sx) dpml 1) 0 0) (size 0
   (* w 2) (* t 2)))))

   ; simulation run
   (run-sources+ (stop-when-fields-decayed
                  50 Ey
                  (vector3 (- (* 0.5 sx) dpml 1) 0 0)
                  1e-5)
                 (at-beginning output-epsilon)
                 )
   (display-fluxes trans) ; print out the flux spectrum
```